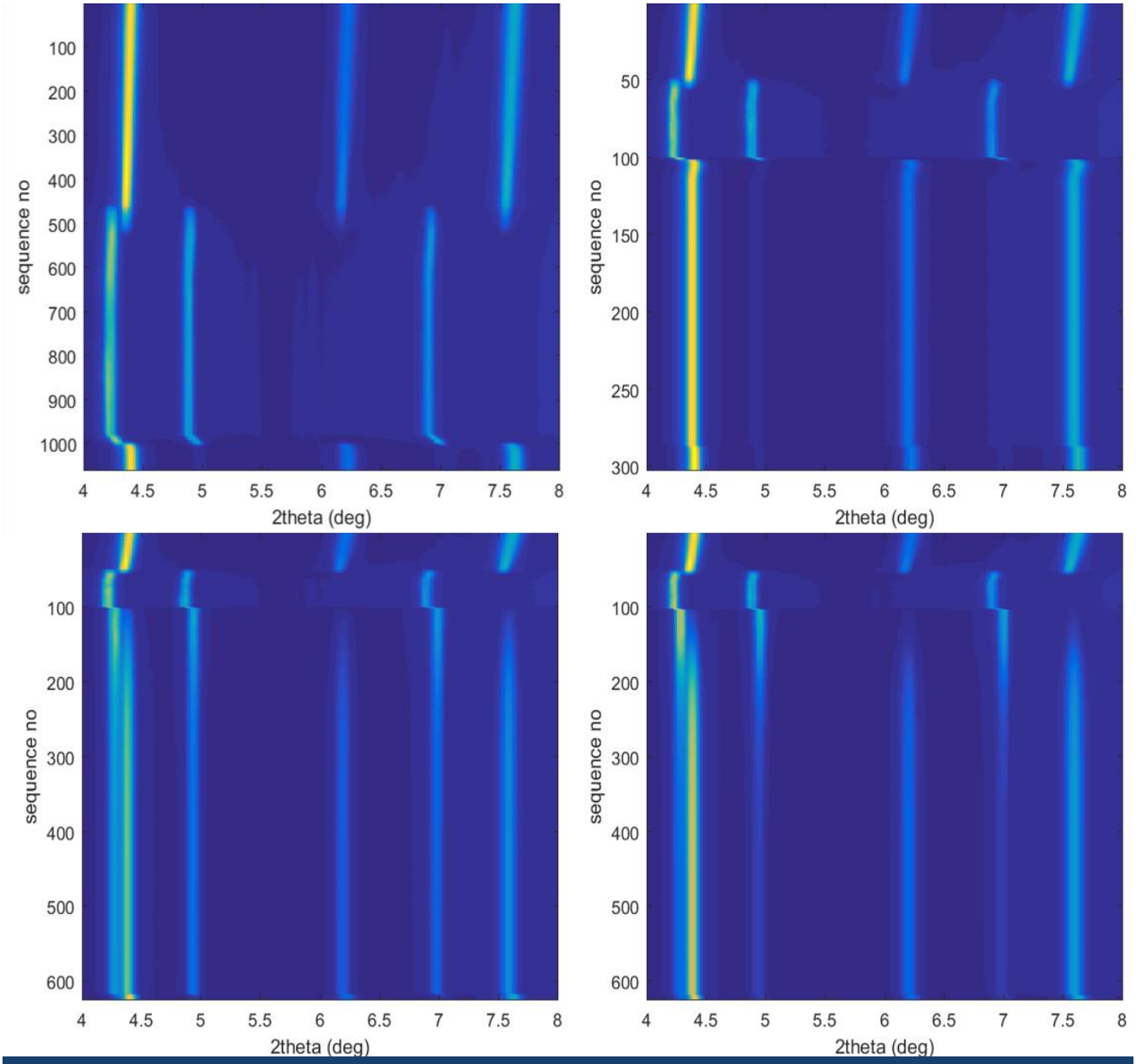

In-situ Synchrotron X-ray Diffraction Study of the Microstructural Development of a Low-C Steel at Low Temperatures

TU Delft

Cholidah Akbar Fitriani 4697316 2019

In-situ Synchrotron X-ray Diffraction Study of the Microstructural Development of a Low-C Steel at Low Temperatures

by

Cholidah Akbar Fitriani

to obtain the degree of Master of Science

at the Delft University of Technology,

Student number:	4697316
Supervisor:	Prof. Dr. Maria J. Santofimia
	Dr. Javier Hidalgo Garcia
	Ir. Alfonso Navarro-López

TU Delft

Acknowledgements

In the name of Allah, the Most Gracious, the Most Merciful.

By submitting this thesis, my learning journey at the Delft University of Technology has come to an end. This journey was not always smooth sailing but the support from all the people around me was able to calm the rough sea. In this short section, I would like to express my gratitude to those people who have helped me through this part of my life, especially in the completion of my thesis.

First of all, I would like to give my supervisor, Prof. Maria Jesus Santofimia Navarro, my sincerest gratitude. Your encouragements during our meetings really fired me up in doing this project as best as I could. With your critical questions, I learned to find solutions from every possible point of view. Thank you for your patience in handling my habit of rushing into things.

At the beginning of this project, I knew nothing about the synchrotron experiments done for this thesis. However, in the end, I was able to analyse the data from the synchrotron experiments thanks to my daily supervisor, Ir. Alfonso Navarro-López. With his detailed insights, I was able to have a clear picture of the synchrotron experiments as if I performed them myself. Thank you for sharing your computer and your office for our additional meetings.

I would like to thank Dr. Javier Hidalgo Garcia for also taking a role as my daily supervisor. I am really grateful for your enthusiasm in transferring your knowledge regarding the data analysis of the synchrotron experiments. Thank you for helping me in elaborating my ideas in a clearer way.

This thesis could not have been possible without the help from Richard Huizenga. Thank you for helping me in one of the most important parts of this project, the coding. Without your help, I would not be able to have those thousands of correctly fitted peaks, thousands of data rows, and those interesting 3D graphs.

I also gratefully acknowledge the full financial support of the Indonesian Endowment Fund for Education (LPDP) which allowed me to pursue a master degree at the Delft University of Technology.

For my cheeriest friends: Ocson Reginald and Sumbranang Adhiwiguna, thank you for keeping up with all my random and sudden talks and requests in the last two years. Thank you also for Muhamad Huba for the sweet treats every now and then.

Last but not least, my whole-hearted and warmest gratitude is for my family. Thank you for the never-ending prayers, endless love, and continuous encouragements.

Cholidah Akbar Fitriani

Delft, June 2019

Abstract

Steel industry is continuously developing novel steel grades for new applications. These newly developed steel grades are based on increasingly complex multiphase microstructures, which is the case of carbide-free bainitic (CFB) steels. Generally, bainitic steels are formed through isothermal treatments at a temperature near (above or below) the martensite start (*Ms*) temperature.

Based on the literature, isothermal treatment below *Ms* can give several advantages over isothermal treatment above *Ms*. One of the advantages is that bainite formation rate during isothermal treatments at temperatures slightly below the *Ms* temperature is significantly higher than at temperatures above *Ms*. However, the precise microstructural developments during isothermal treatments below the *Ms* temperature remain unclear due to the concurrency of several microstructural processes such as tempering of martensite and bainite fsormation.

Microstructural evolutions during heat treatment of steel have been generally studied employing post-processed (ex-situ) characterisation methods. However, the data obtained cannot describe the kinetics of the transformation processes (in-situ) itself. With several microstructural processes happening simultaneously during an isothermal treatment below *Ms*, an in-situ characterisation method which can provide information on the microstructure development is needed. In this regard, Synchrotron X-ray Diffraction (SXRD) method is found to be a suited method.

This thesis aims to study the microstructural developments during isothermal treatments below the *Ms* temperature by in-situ SXRD measurements in a model alloy of composition Fe–0.2C–3.51Mn–1.52Si–0.25Mo (wt.%). To help with the identification of martensite and bainite which have both a body-centre-cubic (BCC) crystal structure, two additional heat treatments were studied by in-situ SXRD: (i) a direct quenching treatment followed by an isothermal treatment to study the tempering of the martensite, and (ii) an isothermal treatment above *Ms* to investigate bainite formation in the absence of martensite. The findings from these heat treatments were then used for studying the microstructural development below *Ms*.

Results from this study show that during the isothermal treatment below *Ms*, bainite was formed right after the isothermal treatment started, which supports previous dilatometry experiments. During the isothermal treatment below *Ms*, four processes are suggested to occur simultaneously: (i) carbon redistribution processes from martensite, (ii) formation of bainite at the martensite/austenite interface, (iii) formation of bainite at the austenite/austenite interface, and (iv) carbon redistribution processes associated with bainite formation. The carbon redistribution processes from the BCC structures are found to occur through carbon partitioning to the austenite, carbon segregation at the dislocation and carbon precipitation to form carbides. However, the two latter processes cannot be differentiated from each other in the current study.

Keywords: isothermal treatment below *Ms*, synchrotron XRD, low C steel, microstructural developments, austenite carbon enrichment

Table of Contents

List of Figures

List of Tables

1

Introduction

1.1 Advanced High Strength Steels

The steel industry is currently facing several challenges: for example, the need to become more energy efficient, environmentally "greener", and less capital intensive [1]. In addition to that, the competition from non-ferrous metals and non-metallic materials is intensifying. The customer's demands to increase the quality and the need to reduce the production cost is driving the industry to produce steels with a better and broader range of desired properties at a low overall cost. To meet these challenges, the steel industry in collaboration with academic communities has been intensively developing new steels within the family of advanced high strength steels (AHSS).

AHSS possess a pleasing combination of strength and formability. AHSS achieve their unique mechanical properties through an appropriate chemical composition in combination with carefully controlled processing and heat treatment which results in its final specific mixtures of microconstituents.

The development of AHSS has produced three generations with the third generation still under development. The idea in developing this generation is to give a significant improvement in terms of strength-ductility combination from the first generation but with less addition of alloying elements, hence cheaper than the second generation. In principle, it can be achieved by multiphase microstructures consisting of a high strength phase/constituent (e.g. nano/ultra-fine grained ferrite, martensite, or bainite) in combination with a phase/constituent which can provide ductility and work hardenability such as austenite [2]–[5].

One of the prospective candidates in the third generation of AHSS is carbide-free bainitic (CFB) steel. These steels are based on microstructures containing a mixture of fine bainitic ferrite plates and thin films of carbon-enriched austenite [6]–[8]. The amount of cementite depends on the carbon concentration of the alloy, and it can also be suppressed by adding alloying elements such as Si and Al [9], [10].

Bainitic steels generally are produced by subjecting the steel to thermal cycles, as shown in Figure 1, involving rapid-cooling from fully austenitic temperature and isothermal treatments at temperatures between the bainite start (*Bs*) and martensite start (*Ms*) temperatures [6]. In Figure 1, it can be seen that different isothermal treatment temperature produces different bainitic microstructures. The microstructures found at temperatures above and below *Ms* will be discussed in more details in sections 1.2 and 1.3, respectively.

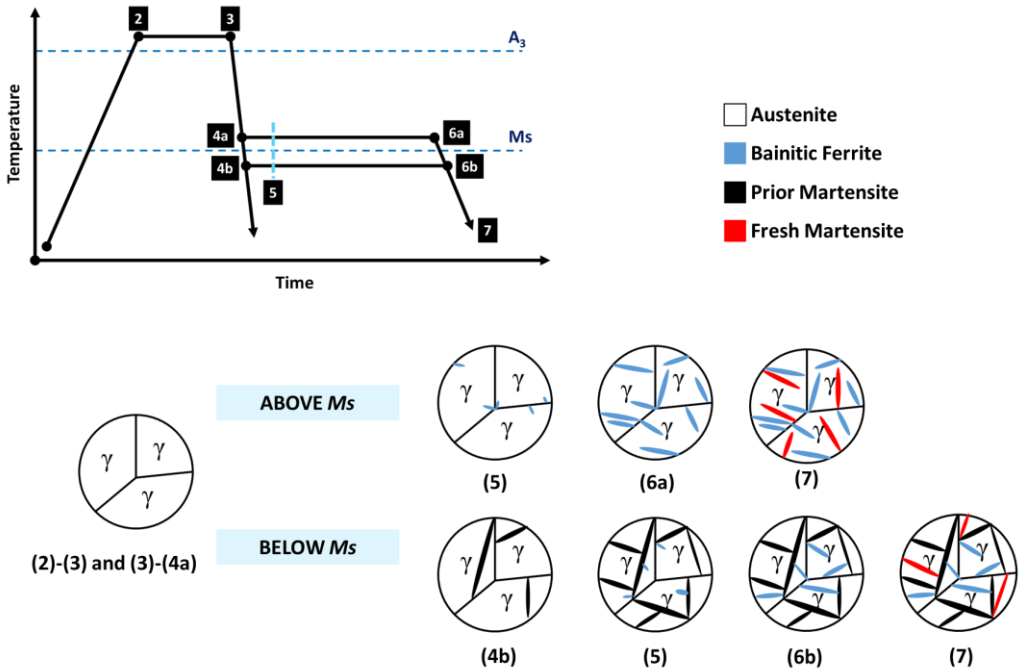

Figure 1 Schematic heat treatments to obtain bainitic steel, (1)-(2) represents heating, (2)-(3): austenitization, (3)-(4a,b): rapid cooling, (4a,b)-(6a,b): isothermal treatment, and (6)-(7): quenching.

As mentioned before, it is possible to achieve simultaneous enhancement of strength and ductility by having bainitic ferrite-austenite microstructures. However, bainitic microstructures often fails to live up the expectation, primarily due to the instability of blocky regions of austenite [11], [12] which will be discussed further in section 1.2.2. Therefore, the aim of the alloy design is to reduce the amount of blocky austenite by increasing the possible amount of bainite, in a commercially viable amount of time [11], [12]. Three mechanisms can be used to increase the amount of bainite formed [13], [14]:

1. By adjusting the type and concentration of the substitutional solutes of the steel
2. By reducing the overall carbon concentration of the steel
3. By minimising transformation temperature

1.2 Microstructures and Phase Transformations at Temperature above *Ms*

1.2.1 Upper and Lower Bainite

Based on the temperature and microstructural features, bainite is identified in two primary forms: upper bainite and lower bainite. Upper bainite is usually formed at temperature range 500°C – 400°C [15] while lower bainite is usually formed at temperature range 400°C – 250°C [15].

As shown in Figure 2, in both upper and lower bainite there is cementite present between the sub-units of bainite. This cementite layer is a product of the transformation of the carbon-enriched austenite surrounding the sub-units of bainite. From the carbon-enriched austenite, ε-carbide is formed and as the isothermal treatment is progressing, the ε-carbide converts into cementite [16]. However, cementite does not necessarily need ε-carbide as a precursor. It is

found that sometimes segregation of carbon in the dislocations is more energetically favourable than their presence in ε-carbide [16]. When the dislocation density of the austenite is high enough, the entrapped carbon in dislocations can directly form cementite from austenite without initiation from ε-carbide.

Besides their similarity, Figure 2 also shows the difference between upper and lower bainite. The primary distinction between upper and lower bainite is that lower bainite has carbide precipitates inside sub-units. This microstructural difference results in different mechanical properties. As a result of carbide precipitation inside the sub-units, there is a fewer cementite layer formed in the lower bainite than in the upper bainite. This condition makes lower bainite tougher and stronger than upper bainite [15].

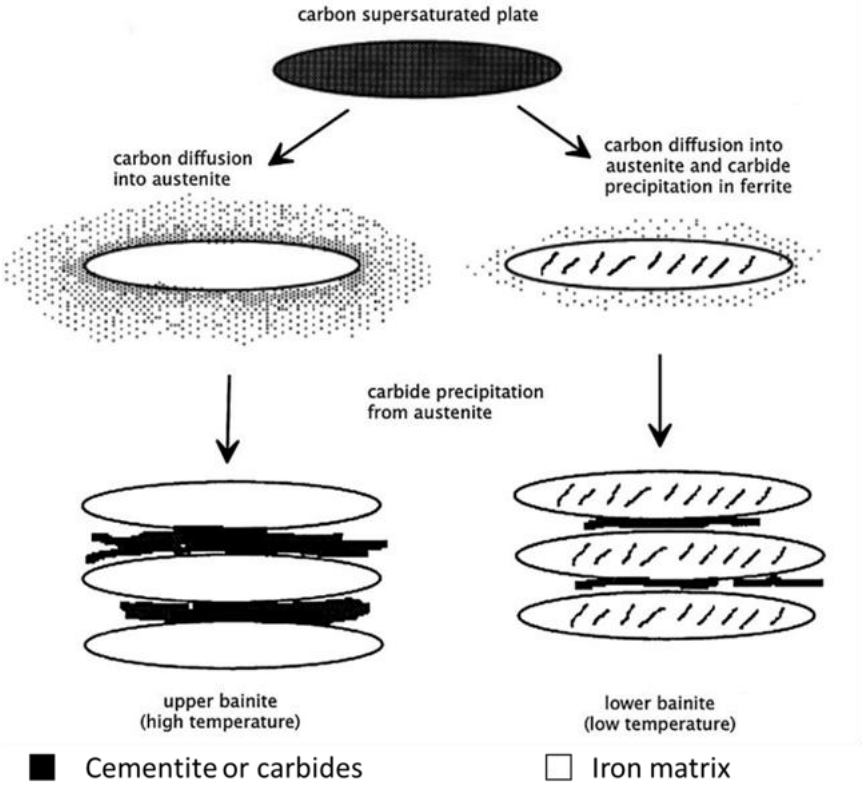

Figure 2 Schematic illustration of the microstructures of lower and upper bainite [15].

1.2.2 Mechanisms of Bainite Formation

There are two major models proposed to describe bainite formation: reconstructive and displacive. The reconstructive model proposes that bainite forms involving the diffusion of atoms as in an eutectoid reaction [17]. On the other hand, the displacive model suggests that bainite formation involves shear as found during martensitic transformation, but with the partitioning of carbon [17]–[19].

Based on the displacive model, the formation and growth of bainitic ferrite are controlled by the T_0' curve which is plotted in Figure 3(a). T_0' curve is the locus of all points, on a temperature versus carbon concentration, where austenite and ferrite of the same chemical composition have

the same energy, taking into account the stored energy of the ferrite due to displacive mechanism from bainite formation [9], [13].

In the displacive model, the formation of bainitic ferrite involves shear causing the structure of bainitic ferrite to be supersaturated with carbon atoms. The excess of carbon atoms trapped inside the bainitic ferrite sub-unit is soon afterwards rejected into the residual austenite. The next sub-unit of bainitic ferrite then has to grow from the carbon-enriched austenite. The growth of bainite can only occur if austenite (the parent matrix) contains less carbon than given by the T_0' curve. The growing of the bainitic ferrite sub-unit must stop when the austenite reaches a carbon concentration indicated by the T_0' curve. Since the carbon concentration of the austenite indicated by T_0' curve is less than the equilibrium carbon concentration of the austenite given by the *Ae3'* curve, the process of bainitic ferrite growth is said to be an incomplete reaction. The schematic illustration of the incomplete reaction can be seen in Figure 3(b).

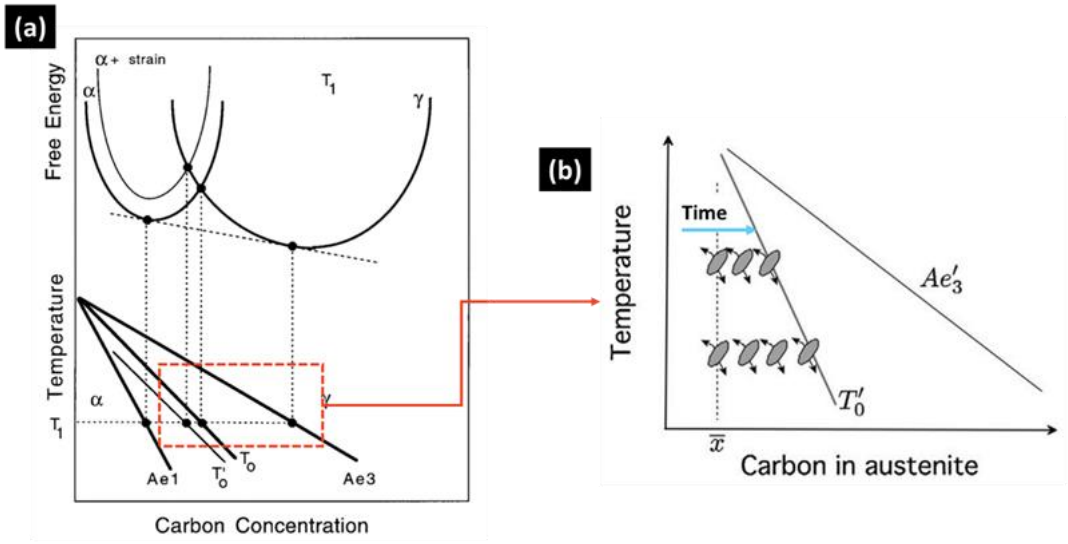

Figure 3 a) Illustration of the T_0' curve which has included the strain energy in the energy curve and b) schematic picture of the incomplete reaction which shows the grow of bainitic ferrite plates until the austenite has reached the C-concentration of the T_0' boundary [13].

During bainite formation, the austenite layer may decompose into ferrite and carbide or cementite if the steel contains strong carbide forming elements [20]. At the end of bainite formation, the residual austenite between bainitic ferrite sub-units may remain as retained austenite layers or may transform to martensite on rapid cooling, depending on its carbon content.

Generally, the retained austenite within bainitic ferrite region appears in the form of small blocks (blocky) austenite or thin films between bainitic ferrite units [7], [21]. Blocky austenite tends to transform to martensite under the influence of small stresses which causes the embrittlement of the steels [22]. On the other hand, filmy austenite is more stable than blocky austenite. There are two reasons behind it: the higher carbon concentration compared to the blocky austenite and the constraint to the transformation to martensite from the surrounding bainitic ferrite plates [11].

1.2.3 The Kinetics of Bainite Formation

Bainitic ferrite sub-units nucleate at austenite grain boundaries and lengthen at a certain rate [15], [23]. A new sub-unit then nucleates from its tip, and as the process continues, the sheaf structure is formed as shown in Figure 4(a). The growth rate of the individual sub-unit is reported to be faster than expected from a diffusion-controlled growth but slower than that of the martensite formation (diffusionless growth) [15].

The nucleation and growth of bainite have several recognised features as reported from the literature [15], [23]–[26]. Isothermally, it starts with an incubation period during which no transformation is detected. The incubation period is then followed by an increase in the rate of transformation until the bainite formed reaches its maximum value. The kinetics is then gradually slowing down. The features in the formation of bainite are schematically pictured in Figure 4(b).

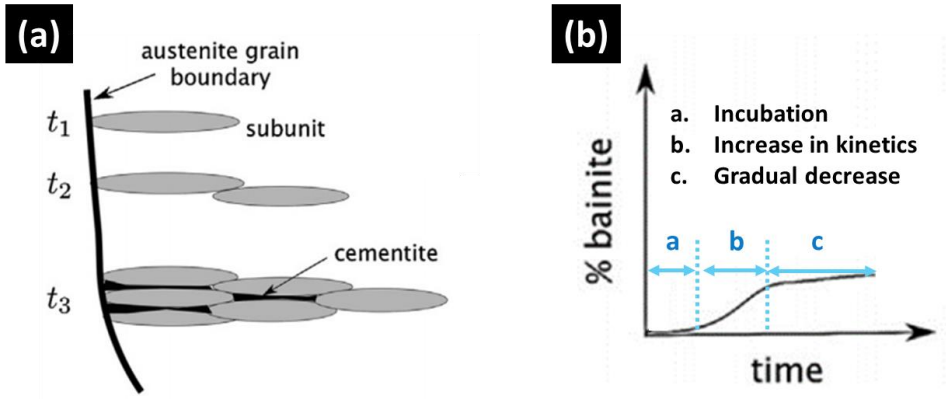

Figure 4 a) Growing process of bainite and b) schematic picture which shows the features of bainite formation and growth: incubation period, an increase in the kinetics, and a gradual decrease in the formation rate [27].

1.3 Microstructure Evolution at Temperatures below *Ms*

1.3.1 Martensite Formation and Tempering

Martensite is a non-equilibrium micro-constituent which is formed when austenite is rapidly cooled (quenched) to a temperature below the *Ms* temperature. The quenching rate is rapid enough to prevent diffusion of carbon atoms. This condition causes a large shear and volume expansion in the transformed region. The martensitic transformation commonly occurs athermally which means that the fraction transformed depends on the undercooling below the *Ms* temperature [23].

Upon isothermal treatment, this martensite undergoes tempering. Tempering is a process in which a non-equilibrium and unstable structure such as martensite becomes closer to equilibrium condition upon heating [28]. The character of the processes that occur during tempering is controlled by three features of the quenched steel: the carbon supersaturation condition within martensite structure, the high density of crystal lattice defects such as

dislocations and internal stresses introduced due to martensite formation, and the presence of retained austenite [27], [28].

During tempering, the high carbon supersaturation in the martensite acts as a driving force for carbon segregation and carbide precipitation. The high dislocation density creates sites for carbon segregation and carbide precipitations. In addition to that, the internal stresses following the formation of martensite may be relieved during tempering [29]. Last but not least, any retained austenite must transform into equilibrium phases, i.e. ferrite or bainite, during tempering. Furthermore, some carbon atoms from the martensite may also partition to the austenite and stabilise the retained austenite [30]–[32].

Steel with high *Ms* temperature, such as low carbon steels, often shows auto-tempering. Auto-tempering is a formation of cementite from the first formed martensite (martensite formed near *Ms*) during the remainder of the quench [31]. It is due to the high temperatures below *Ms* that allow diffusion of carbon atoms for forming cementite [27].

1.3.2 The Accelerated Formation of Bainite

It is known that the formation of bainite below *Ms* is possible [33]. In the study by Silva et al. [34] the decomposition of austenite in low carbon steel during isothermal treatment below *Ms* was investigated. Observations using dilatometry were performed during the study while the characterisation of the final products was carried out by Scanning Electron Microscopy (SEM) and Electron Backscatter Diffraction (EBSD). The dilatation curves from this study show that, for isothermal treatment below *Ms*, martensite was formed during cooling before reaching the designated isothermal temperatures. The transformation then progressed rapidly in the first minute of isothermal holding which by the author was assumed to be coming from bainite formation.

A study by Navarro-López et al. [21], [35] shows that for low-C steel, the nature of the isothermal product formed below *Ms* temperature is bainitic ferrite. In their study, they reported the morphological features observed using SEM and EBSD which can be used to distinguish between an isothermal product with martensitic nature and an isothermal product with bainitic nature.

In the study by Samanta et al. [33], it is clearly stated that for a low-C steel, the phase transformations that occurred in isothermal treatment below *Ms* is only bainite formation. This conclusion was supported with the kinetics of the isothermal transformation, which was showed to be consistent with an existing model of bainite transformation based on the displacive theory. In the study, the kinetics model of isothermal martensite formation was proved to be not possible for their studied alloy system.

Contrary to this finding, the research by Kim et al. [36]–[38] suggests that for low carbon steel, the product of the phase transformations which occurred isothermally below *Ms* is neither purely bainitic nor purely martensitic. The isothermal product formed below *Ms* was observed to have a similar transformation rate to that of athermal martensitic transformation. However, the isothermal transformation below *Ms* proceeds by the lateral advancing of the interface rather than the formation of new laths, as in the case of athermal martensite. The internal friction measurements showed that the solute carbon content of the isothermal products formed below *Ms* temperature is between those of athermal martensite and lower bainite.

In addition to that, in the isothermal treatment below *Ms* temperatures, the formation of martensite prior to the treatment is unavoidable. During isothermal temperatures at a temperature slightly below *Ms*, the rate of austenite decomposition into bainite increases significantly [34], [35], [37], [39], [40]. This behaviour is a reversal to the general trend of the decomposition rate of austenite which is retarded with decreasing in temperature. This reversal in kinetics has correlations with the presence of martensite.

Two possible mechanisms can be used to explain the accelerating effect of pre-existing martensite to the bainite formation [41]:

1. The stress induced by martensite transformation accelerates the nucleation of bainite around pre-existing martensite.
2. The austenite-martensite (γ/α') interfaces can act as a potential nucleation site for bainite.

In the study by Kawata et al. [41] the effect of stress induced by the martensite to the acceleration of bainite formation is proved to be small. They reported that the acceleration of formation of bainite depends more on the γ/α' interfaces rather than on the stress induced by the martensite. It was found that the acceleration rate of bainite formation is proportional to the fraction of prior martensite in the steel.

The importance of the γ/α' interfaces in the higher kinetics of bainite formation is then studied further by Navarro-López et al. [35]. In this study, it was reported that the increase in prior martensite accelerated the kinetics of bainite formation. However, the relation between these two parameters is not proportional. The accelerating effect is more closely related to the interfacial area of γ/α' interfaces, i.e. the arrangement of the martensite unit, than the volume fraction of the martensite.

Based on the conditions above, it can be seen that there is still unclarity not only in the nature of the isothermal product formed below *Ms* but also the major factor for the acceleration of the bainite formation during isothermal treatment below the *Ms* temperature.

1.4 Characterisation Method - Synchrotron X-Ray Diffraction (SXRD)

During isothermal treatments below *Ms*, several processes overlap such as the formation of bainite, the tempering of the prior athermal martensite, carbon segregation, precipitation and partitioning of alloying elements. Recent developments in the Synchrotron X-Ray Diffraction (SXRD) technique have enabled to follow not only the progress of the austenite decomposition into micro-constituents such as martensite and bainite, but also the evolution of carbon and stress of each micro-constituent involved [25], [26], [42]–[44].

In recent years, the use of synchrotron as an X-ray source has attracted much attention since it allows rapid measurement of diffraction patterns [43], [45]. The high time resolution of SXRD is achieved through the addition of 2D charge-coupled device (CCD) detectors which allow simultaneous recording of all diffracted crystalline planes. In SXRD, the detectors do not need rotational movement. Thus, the measurement time can be significantly improved. The high energy X-rays used in the synchrotron are able to gain deeper penetration depth and larger sampling volume. Therefore, the SXRD is less sensitive to the surface condition of the sample,

i.e., no excessive polishing needed for the surface of the sample [44]. The schematic representation of the SXRD regarding detectors is shown in Figure 5.

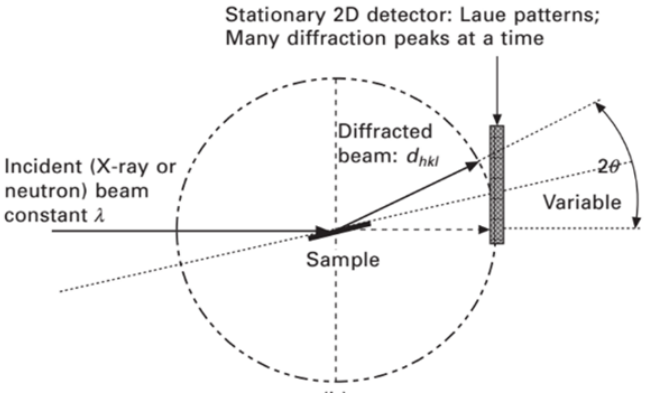

Figure 5 Schematic representation of the sample and detector position found in SXRD which shows the stationary detector [43].

Utilising 2D CCD detectors, the diffraction pattern from a polycrystalline sample forms a series of diffraction cones if a large number of crystals are covered by an incident beam, as shown in Figure 6. Each cone, referred as a Debye ring, represents the diffraction of the same family of a crystalline plane in all participating grain [46]. This diffraction pattern can be obtained at intervals of 0.3 seconds or less [43]. To analyse the microstructural evolution during the treatment, the diffraction images received are calibrated using standard samples. Following that, the diffraction rings are integrated to produce a standard intensity versus diffraction angle (2θ) pattern, also called 1D diffraction pattern [43]. Based on this description, SXRD results to be an attractive method for acquiring time-resolved precise quantitative information about every phase/constituent present in the investigated material [43], [47].

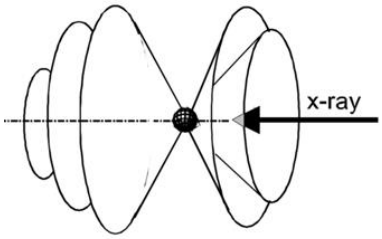

Figure 6 Schematic figure showing diffraction cones obtained from a polycrystalline sample [46].

The fast acquisition time of the SXRD method is proved to be useful in studying the nucleation and growth of steel. Savran et al. [48], in their study of the reverse transformation of the austenite from pearlite, have been able to distinguish between the austenite nucleation which developed from the ferrite-pearlite grain boundaries and the austenite nucleation which developed from ferrite-ferrite grain boundaries based on the data obtained from SXRD method.

Babu et al. [49] also utilised the SXRD method for studying the formation of bainite in high-C steels. In their study, the isothermal kinetics of bainitic ferrite formation are tracked as well as the evolution of the lattice parameter of the austenite and ferrite during the treatment. From this

study, it was found that the lattice parameter of the bainitic ferrite slowly reduces with time as a consequence of carbon partitioning from bainitic ferrite to austenite. They also correlated the change in the austenite lattice parameter with carbon variation. This step led to the finding of simultaneous formation of C-enriched and C-depleted austenite during bainite formation.

In the study by Kolmskog et al. [50], in-situ SXRD was used simultaneously with laser scanning confocal microscopy (LSCM) to confirm the formation of bainite in 0.5 wt.% C steel below the *Ms* temperature. Based on the series of microstructural images from the LSCM and the evolution of interplanar spacing from the {011} planes of BCC structures and {111} planes of FCC structures, they concluded that bainite was formed during the isothermal treatment below *Ms*.

A study about microstructural evolution during isothermal treatment below *Ms* by using SXRD was also performed by Allain et al. [51]. In their study, 0.3 wt% C steel was used for the isothermal treatment below *Ms*. By studying the evolution of the austenite lattice parameter and the evolution of the phase fraction during the treatment, they proposed that the microstructural processes occurring during isothermal treatment below *Ms* are concurrent bainite transformation and carbon partitioning from the prior athermal martensite to the austenite.

Besides assisting the observation of microstructural developments that happen in the steel, SXRD is also proved to be able to evaluate stress accompanying a specific process. Villa et al. [52] used SXRD to evaluate the evolution of lattice strain and stress imposed by martensite to the austenite during quenching and partitioning process. In their study, they were able to prove that stress is built up in austenite during the formation of martensite.

The lower sensitivity to the surface preparation also provides an advantage to the SXRD method especially in the study of multiphase steels [44]. Multiphase steels contain unstable constituents such as metastable retained austenite which may transform into martensite if excessive stress is introduced during the surface preparation stage. SXRD measures bulk properties and is, therefore, less sensitive to surface properties.

1.5 Objectives and Scope of the Thesis

This thesis aims to investigate the microstructural evolutions during an isothermal treatment below the *Ms* temperature with aids primarily from SXRD. In this study, the material used is low-carbon high-silicon steel. The experimental data obtained from SXRD is served the purpose to answer the following research questions:

1. What are the microstructural developments involved during the isothermal treatment below *Ms*?
2. How does the carbon redistribution from BCC constituents to FCC phase occur during the isothermal treatment below *Ms*?
3. What are the effects of the carbon redistribution process from the BCC to FCC to the stability of the retained austenite?

1.6 Research Approach

The formation of bainite below *Ms* implies the presence of martensite formed during cooling prior to the isothermal treatment. Therefore, tempering of martensite and bainite formation occur simultaneously during isothermal treatments below the *Ms* temperature [34], [35], [37].

The concurrence of these reactions makes it difficult to identify the details of the microstructure development taking place during isothermal treatments below the *Ms* temperature. For these reasons, the present study focusses on four different heat treatments aiming to isolate these concurrent mechanisms. These four heat treatments and their corresponding goals are:

1. **Direct quenching treatment,** to identify the characteristics of the formation of athermal martensite.
2. **Quenching and tempering treatment,** to identify mechanisms associated with the tempering of martensite.
3. **Isothermal treatment above *Ms*,** to identify the characteristics of the formation of bainite.
4. **Isothermal treatment below *Ms***, to identify the microstructural development during isothermal treatment below *Ms*.

The features observed in the first three treatments can be used as key factors for identifying the mechanism that takes place during the isothermal treatment below *Ms* in the fourth heat treatment.

1.7 Structure of the Thesis

This thesis comprises four chapters with the first chapter addressing the background and the objectives of this research. Chapter 2 describes the experimental procedures carried out in the study. Chapter 3 presents the analysis of the results found in this study followed by chapter 4 which summarises the conclusions and recommendations of this study. At the end of this manuscript, an Appendix is attached for the relevant data obtained in this study.

2

Material and Experimental Methods

2.1 Material

The chemical composition of the low carbon steel used in this research study is shown in Table 1. The low carbon content is chosen since low-C steel has better weldability than high-C steel [10], [53]. Manganese (Mn) stabilises austenite, delaying the formation of ferrite, martensite or bainite during the first cooling [6], [10]. In addition to that, austenite decomposition to ferrite phase is also retarded by the addition of Mo [10], [54]. Addition of Si has the objective to inhibit the formation of cementite [10], [55].

The material was received in the form of a hot-rolled slab of 4 mm thickness. From the slab, double T-shaped specimens, as pictured in Figure 7, were machined and used for all the SXRD measurements.

Table 1 The chemical composition of the low-C steel used in this work

Element	C	Mn	Si	Mo	N	S	P
wt.%	0.2	3.51	1.523	0.247	0.0039	0.0069	0.005

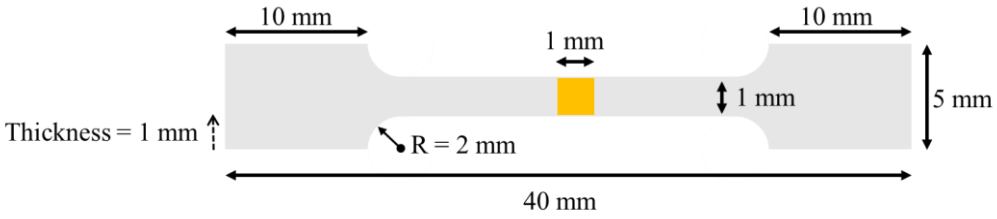

Figure 7 Dimension of the specimen used in the SXRD measurements. The yellow box represents the detection area for the X-ray beam.

The transformation temperatures of this material can be calculated from the empirical equations written in Equations (2-1)-(2-3) [56]. In these equations, x_i corresponds to the weight percent of the element "*i*" in the steel. The results of the calculations of the transformation temperatures are summarised in Table 2.

$$\boldsymbol{Ac_1}(^0C) = 739 - 22x_C + 2x_{Si} - 7x_{Mn} + 14x_{Cr} + 13x_{Mo} - 13x_{Ni} \quad (2\text{-}1)$$

$$\boldsymbol{Ac_3}(^0C) = 902 - 255x_C + 19x_{Si} - 11x_{Mn} - 5x_{Cr} + 13x_{Mo} - 20x_{Ni} + 55x_V \quad (2\text{-}2)$$

$$\boldsymbol{Bs}\ (^0C) = 656 - 57.7x_C - 35x_{Mn} - 75x_{Si} - 15.3x_{Ni} - 34x_{Cr} - 41.2x_{Mo} \quad (2\text{-}3)$$

In Equation (2-1) and (2-2), Ac_1 and Ac_3 are the lower and the upper ferrite-austenite transformation temperatures, respectively. Based on dilatometry experiments done by Navarro-López [35] in the same steel, the *Ms* temperature is equal to 320°C ± 5°C.

Table 2 The calculated transformation temperatures of the investigated steel.

No.	Transformation Temperature	Value (°C)
1.	Ac_1	716 (calculated)
2.	Ac_3	844 (calculated)
3.	Bs	397 (calculated)
4.	Ms	320 (measured [35])

Utilising Thermocalc® software with TCFE8 database and limiting the stable phases to austenite, ferrite, and carbides, the evolution of the amount of the phases can be calculated which is presented in Figure 8. Based on this figure, it can be seen that at a temperature lower than 600°C, besides BCC phase (ferrite phase), the formation of transitional carbides (M_7C_3 and M_6C) are energetically favourable despite the addition of 1.5 wt.% of Si.

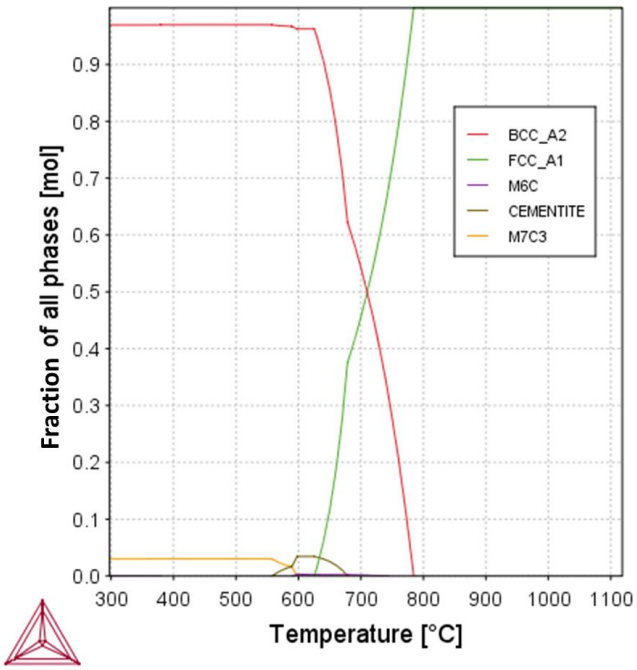

Figure 8 Evolution of fraction of phases of the studied steel calculated using Thermocalc®.

2.2 Heat Treatments

Before subjected to the heat treatments, all specimens were pre-treated by homogenization at 1250°C for 48 hours in a furnace with a protective atmosphere to reduce the Mn-segregation. In order to avoid the formation of large austenite grains, samples were quenched two times in a salt bath solution from a fully austenitic temperature of 900°C. This step was essential to avoid the

formation of spotty rings in diffraction patterns due to the presence of the big austenite grains. The spotty rings are unwanted as they can affect the fitting of the diffraction patterns [57]. At the end of the second quenching, the sample consisted of fine martensite grains. The pre-treated samples were then ready to be subjected to subsequent heat treatments.

The heat treatments performed during in-situ SXRD measurements are illustrated in Figure 9. One thermocouple was spot-welded at the centre of the gauge length of all samples to control the temperature during the heat treatment, which was carried out under a protective atmosphere of argon gas to minimise sample oxidation. All heat treatments described in Figure 9 started with heating at a rate of 2°C/s to a 900°C, which is above the Ac_3 temperature. The sample was then austenitized for 240 s to form a fully austenitic structure as well as to homogenise the chemical composition. Following austenitization, the sample was rapid-cooled to the selected temperatures, depending on the treatments, with 40°C/s as the cooling rate.

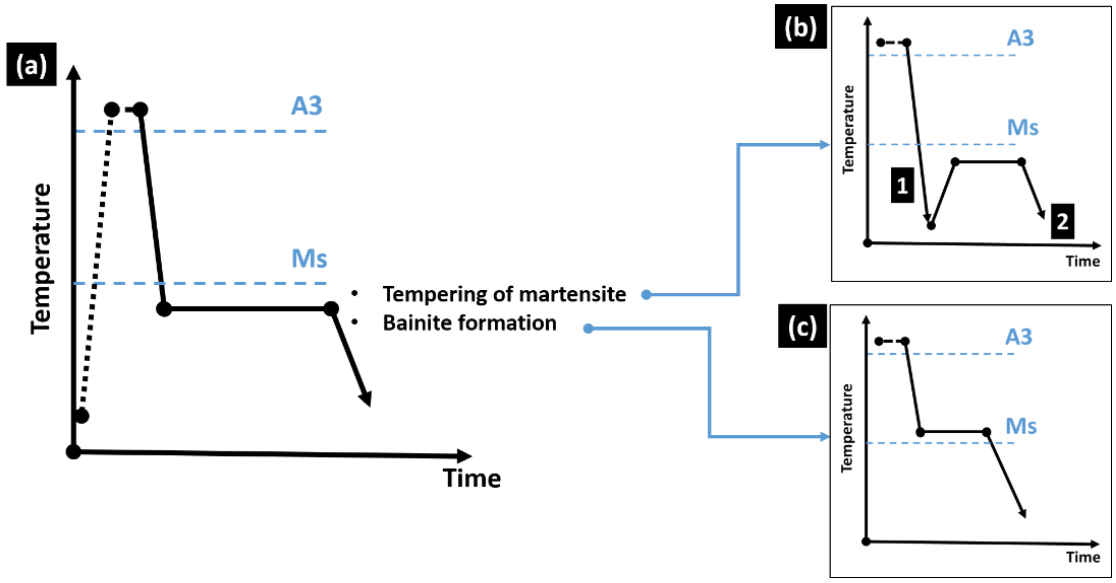

Figure 9 Heat treatments carried out in the study which consist of a) an isothermal treatment below Ms, b.1) a direct quenching treatment, and b.2) a tempering treatment. The characteristics of bainite formation are identified through observation in c) an isothermal treatment above Ms.

1. **Isothermal Treatment Below *Ms* (Figure 9(a))**
   The primary objective of this research study is to identify the processes that occur at the isothermal treatment below *Ms.* Thus, the isothermal treatment depicted as the cycle (a) in Figure 9 was designed. The material was isothermally treated at 305°C for 3600 s. After isothermal treatment, the sample was cooled down to room temperature with 20°C/s as the cooling rate.

2. **Direct Quenching and Tempering Treatment (Figure 9(b))**
   The objective of a direct-quench is to identify the features in SXRD data that accompany the formation of martensite. These features include changes in phase fraction, changes in austenite and martensite lattice due to strains introduced during the martensite formation, and interstitial carbon segregation/partitioning during tempering. Direct quenching treatment is figuratively described as the cycle (b.1) in Figure 9.

Serving the purpose to identify the features of the tempering of martensite, the quenching was followed by a tempering treatment. The tempering stage was performed at 305°C for 20 minutes, the same temperature used for the isothermal treatment performed below *Ms*. The sample was then cooled down with a cooling rate of approximately 20°C/s. The tempering process is schematically depicted as the cycle (b.2) in Figure 9.

3. **Isothermal Treatment Above *Ms* (Figure 9(c))**
   The objective of isothermal treatment above *Ms* is to identify features in the SXRD spectrums which follow the bainite formation. After austenitization, the sample was rapid-cooled at 40°C/s followed by an isothermal treatment at 350°C for 1 hour. After isothermal treatment, the sample was cooled down to room temperature at 20°C/s. The isothermal treatment above *Ms* is schematically described as the cycle (c) in Figure 9.

2.3 In-situ Characterization: SXRD

The characterisation method used to analyse the processes during the application of heat treatments was Synchrotron X-Ray Diffraction (SXRD). SXRD experiments were performed at the European Synchrotron Radiation Facility (ESRF) in Grenoble, France. The incident beam used in this study has a wavelength of 0.15582 Å, beam size of 200×200 μm, and energy of 79.57 keV.

The diffraction rings were obtained by a Frelon CCD camera with a detector distance (*D*) equal to 300 mm. The images collected have 2048 × 2048 resolution with 50 × 50 μm pixel size. To take an image, the exposure time chosen was 0.1 seconds and the time interval from one diffraction ring to the subsequent ring was approximately 0.7 seconds.

Before commencing the in-situ SXRD measurement, cerium oxide (CeO_2) was used as a calibrant to obtain the relevant instrumental parameters such as sample-to-detector distance, beam centre, and tilted angle of the detector. The time of exposure for the calibrant was 60 seconds. The in-situ SXRD measurement is schematically described in Figure 10.

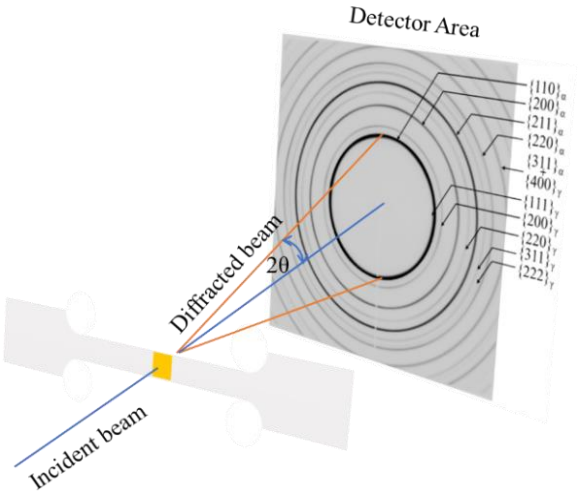

Figure 10 Schematic illustration of the SXRD measurements.

2.4 Data Analysis for SXRD

The raw data obtained from the SXRD measurements cannot directly be used to study the processes that occur during the heat treatments. This data is initially in the form of 2D diffraction patterns which are needed to be converted into standard 1D patterns, intensity (I) as a function of the diffraction angle (2θ), for further analysis. The analysis process for SXRD is schematically described in Figure 11, which shows that the data analysis of the 2D diffraction pattern can be divided into three main stages [43]:

1. **Calibration and determination of detector characteristics and experimental geometry**
   The 2D CCD detector measures the whole Debye ring of the sample, as shown in Figure 11(a), and after that, the geometry of the detector with reference to the diffraction geometry must be calibrated [43], which is performed using a cerium oxide (CeO_2) standard reference sample. This calibration was done by fine-tuning the distance between detector and sample, X-ray wavelength, beam centre, the rotation angle of the tilting plane, and the angle of the detector in that plane [43], [58]. The calibrations were performed using the Fit2D software.

2. **Integration of the Diffraction Rings**
   This stage involves the integration of the Debye rings obtained during the treatments. These integrations were calculated using the Fit2D software. The 2D diffraction patterns collected directly from SXRD are converted into the standard 1D spectrum by integrating them along the scattering angle (2θ) over the selected azimuth angles (η). From this stage, the data can be collected into an image format showing the diffraction intensity of the different peaks as a function of temperature and time, as shown in Figure 11(b).

3. **Peak Fitting and Analysis**
   In this stage, the area under each diffraction peak is analysed using an automated peak fitting and analysis routines software. In this study, the peaks of interest are the peaks from $\{200\}_\gamma$ and $\{220\}_\gamma$ planes of the austenite (FCC) and peaks from $\{200\}_\alpha$ and $\{211\}_\alpha$ planes of the bainite/martensite (BCC). These four peaks are extracted from the original 1D diffraction pattern. The fitting process of these four peaks is shown in Figure 11(c). The properties of each peak (height, width, position, etc.) are then calculated, and the results are recorded in a worksheet as shown in Figure 11(d). This data is then used to track the microstructural evolution that happens as a function of temperature and time.

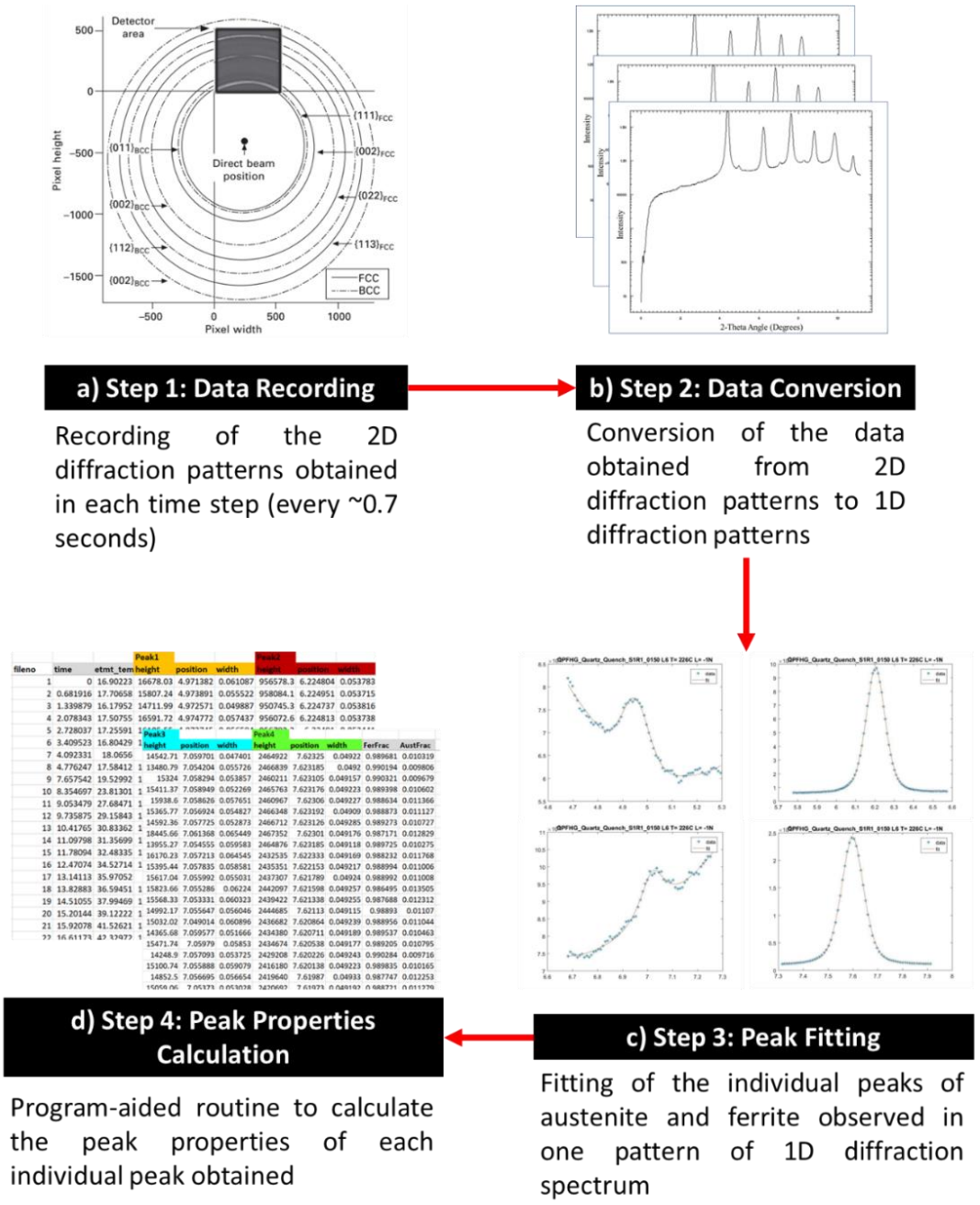

Figure 11 Steps involved in the analysis of SXRD data.

As mentioned previously, the first step in peak fitting and data analysis is separating the four peaks of interests from one image of a 1D spectrum as shown in Figure 12(a) into four different 1D spectrums as shown in Figure 12(b). Each 1D spectrum is then fitted to a pseudo-Voigt function to obtain the first peak property which is the peak position or 2θ. From Figure 12, it can be seen that the first peak of FCC which is {111} and the first peak of BCC which is {110} are not included in the analysis as these peaks overlap with each other and these peaks correspond to the lowest information depth; thus are the most sensitive to the surface effects [52].

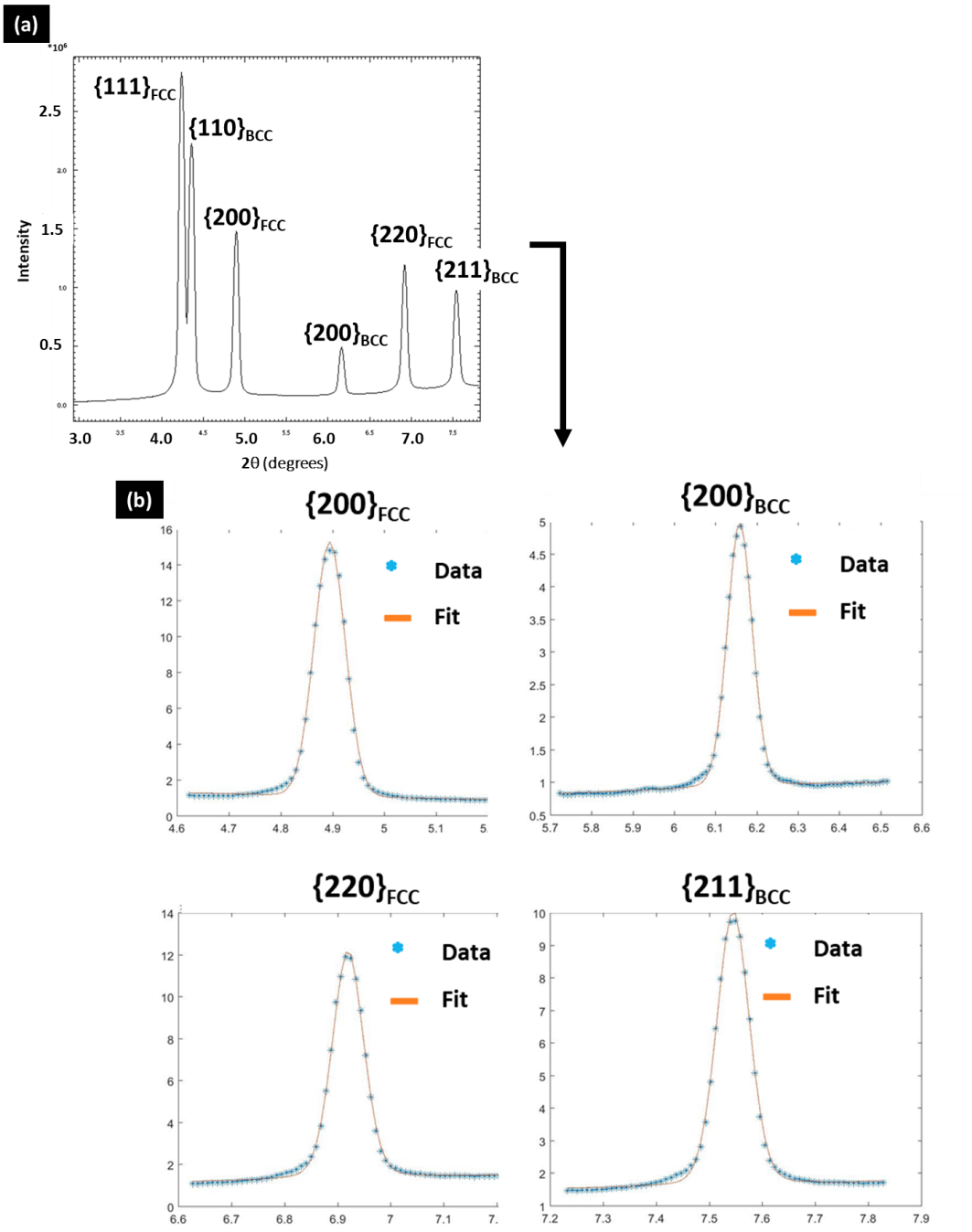

Figure 12 a) The primary 1D spectrum-images which contain several peaks from different planes and structures and b) four different 1D spectrum images extracted from one primary 1D spectrum-images on the left.

Figure 13 shows the general 1D diffraction pattern that can be obtained from SXRD measurement. In Figure 13, there are two essential peak properties shown: peak area and peak position. The details of each property are as follow:

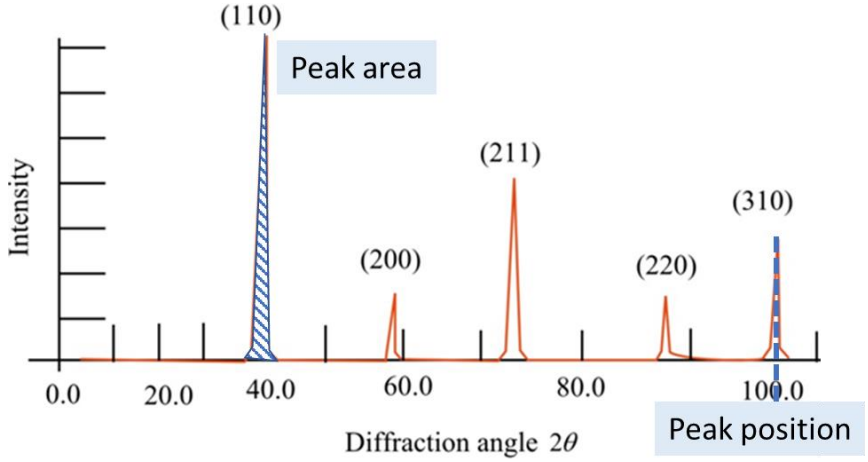

Figure 13 Peak properties that can be extracted from the 1D diffraction pattern: peak area, peak height, and peak position.

1. **Peak area**

   The peak area is a property calculated from the integration of the total intensity under a peak. By comparing the peak area of a particular phase with the total peak area observed in the spectrum, the volume fraction of the particular phase in the mixture can be obtained [59], [60]. In this work, the volume fraction of the retained austenite is estimated using Equation (2-4) [59].

$$f_\gamma = \frac{\frac{1}{N}\sum_{i=1}^{N}\left(\frac{I_{\gamma,i}}{R_{\gamma,i}}\right)}{\frac{1}{N}\sum_{i=1}^{N}\left(\frac{I_{\gamma,i}}{R_{\gamma,i}}\right)+\frac{1}{M}\sum_{i=1}^{M}\left(\frac{I_{\alpha,i}}{R_{\alpha,i}}\right)} \tag{2-4}$$

   where $I_{\gamma,i}$ and $I_{\alpha,i}$ are the integrated intensity (peak area) of the monitored austenite and ferrite peaks, respectively. *N* and *M* are the numbers of considered austenite and ferrite peaks, respectively. The index *i* refers to the Miller indices (*{hkl}*) of the peak of interest. $R_{\gamma,i}$ and $R_{\alpha,i}$ are the normalisation factors for the austenite and ferrite, respectively. The value of these normalisation factors depends on the interplanar spacing (d_{hkl}), Bragg's angle (θ), crystal structure, and phase composition [61]. The details for the calculation of R-factors are described in the study of van Dijk et al. [59]. It is worth to note that these factors are calculated considering a random orientation of phases. Texture will also influence the relative intensity of peaks and if this happens, it has to be considered adequately.

2. **Peak position**

   The peak position is equal to the diffraction angle (2θ) of the specified plane. The data about peak position is the primary source for calculating the lattice parameter changes in both the BCC and FCC phases. According to Bragg's Law written in Equation (2-5) [29]. The diffraction angle (θ) can be related to the interplanar spacing of the refracted plane d_{hkl} as written below

$$n\lambda = 2d_{hkl} \sin\theta \tag{2-5}$$

where *n* is the order of reflection, which is equal to 1 and λ is the wavelength used in the characterisation and for this study is equal to 0.15582 Å. The relation between variables in Bragg's law is illustrated in Figure 14 [29].

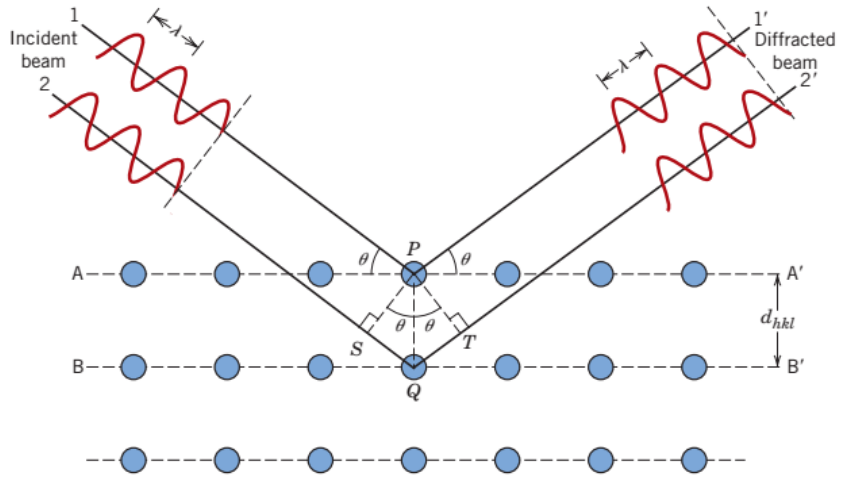

Figure 14 Schematic description of X-ray diffraction by planes of atoms in a solid [29].

The value of interplanar spacing (d_{hkl}) is a function of the Miller indices of the involved planes and the lattice parameter a according to [29]:

$$d_{hkl} = \frac{a}{\sqrt{h^2 + k^2 + l^2}} \tag{2-6}$$

By combining Equation (2-5) and Equation (2-6), the value of the lattice parameter at a specific temperature and time can be calculated from the peak position (2θ) value.

2.5 Microstructural Properties Derived from the Peak Properties

2.5.1 Carbon Content of the Austenite

It is known that the lattice parameter of the austenite is influenced by its carbon content. Babu et al. [49] suggested Equation (2-7) to quantify the change in the austenite lattice parameter due to carbon variation in the austenite. In the Equation (2-7), x_i corresponds to the weight percent of the element "*i*" in the steel.

$$a_{FCC}\,(\text{Å}) = 3.578 + 0.033x_C + 0.00095x_{Mn} + 0.0006x_{Cr} + 0.0031x_{Mo} - 0.0002x_{Ni} + 0.0018x_V + 0.0056x_{Al} \tag{2-7}$$

2.5.2 Carbon Content of the Martensite

As a product of the displacive transformation, the chemical composition of martensite is the same as the chemical composition of its parent austenite. Therefore, the lattice parameter of martensite might also be affected by the carbon content as that of austenite lattice parameter

[49], [61]–[63]. Hidalgo et al. [61] in their study mentioned that the martensite lattice parameter is affected by its carbon content which is defined by

$$a_{\alpha'}\,(\text{Å}) = 2.866\ \text{Å} + \frac{x_C}{31\,\frac{wt.\,\%}{\text{Å}}} \tag{2-8}$$

with $a_{\alpha'}$ is the measured lattice parameter (Å) of the martensite calculated using Equation (2-5) and (2-6), x_C corresponds to the weight percent of the carbon in the steel, and 2.866 Å is the reference lattice parameter of the BCC lattice without carbon at room temperature.

2.5.3 Experimental Coefficient of Thermal Expansion (CTE)

Generally, most solids expand when being heated which means that the value of interplanar spacing (*d*) in the space lattice increases. The mean linear coefficient of expansion of a solid (α_m) is defined by [64]

$$\alpha_m = \frac{1}{L_1}\frac{L_2 - L_1}{T_2 - T_1} \tag{2-9}$$

where L_1 and L_2 are the corresponding length (measured in meter) at a temperature T_1 and T_2 (measured in Kelvin). Therefore, the differential coefficient of thermal expansion $\alpha(T)$ (CTE) can be written as

$$\alpha(T) = \frac{1}{L(T)}\frac{dL(T)}{dT} \tag{2-10}$$

with *L(T)* is a length at temperature *T*.

The differences in the lattice parameter (*dL(T)*) and temperature (*dT*) with respect to the reference lattice parameter and the reference temperature were then calculated in each temperature step measured during heating or rapid cooling stage. The gradient of the trend line of $\frac{1}{L(T)}dL(T)$ as a function of temperature is then equal to the coefficient of the thermal expansion of the measured phase.

Based on the evolution of the martensite lattice parameter during the heating stage and the evolution of the austenite lattice parameter during the rapid-cooling stage, the CTE of martensite and austenite can be calculated. In the calculation of CTE, the CTE of $\{200\}_\alpha$ and $\{211\}_\alpha$ planes of the martensite are differentiated since each plane has its own peak position and change in the martensite lattice parameter may also different. For the same reason, the CTE of $\{200\}_\gamma$ and $\{220\}_\gamma$ planes of the austenite are also differentiated. One of the examples of the CTE calculation for the austenite is shown in Figure 15.

After choosing the appropriate heat treatment stage, a temperature range for the calculation of the CTE must be defined.

1. **Martensite**
   In this study, the temperature range for calculating the CTE of martensite is defined between 16ºC – 600ºC of the heating stage. There are two reasons for choosing this temperature range:

a) The temperature range is lower than Ac_1 which for this study is equal to 716ºC as written in Table 2.
b) The peaks of austenite are absent in this temperature range, as observed in the diffraction spectrums. Thus, the dominant microstructure is martensite.

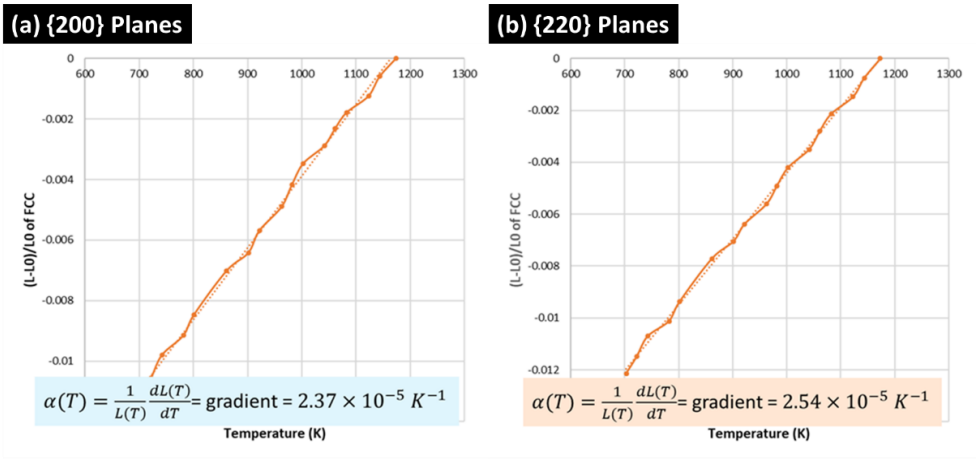

Figure 15 The calculation of the CTE of the austenite for a) {200} planes and for b) {220} planes.

2. Austenite

The calculation of the CTE of the austenite was done for a temperature range between 400°C – 900°C of the rapid-cooling stage. There are also two reasons for using this temperature range which are:

a) The limit temperature of 400ºC is still higher than the *Ms* temperature, which based on the dilatometry experiment [35] is measured around 320ºC. Therefore, no martensite (BCC structure) presents in the range.
b) Observation on the diffraction patterns shows that, in this temperature range, there are only austenite peaks, so a fully austenitic condition is achieved.

2.6 1D Peak Fitting Analysis: Challenges

In order to obtain the properties of each microstructure involved in each heat treatment, after steps mentioned in section 2.4, a set of peak properties data related to each heat treatments are calculated. The process to obtain the peak properties is a program-aided routine. However, at a particular condition, the program may fail to give correct peak properties. In order to have a correct data set, each data point is again evaluated with its corresponding 1D (I vs 2θ) spectrum. In this section, the conditions that often cause incorrect peak fitting are discussed.

2.6.1 Peak Finding in the Absence of Crystal Structure

In this study, failure to give reliable data is usually found when the specified structure (BCC or FCC) is not present yet or forms in a significantly low volume fraction. Three temperature ranges met this description:

1. During heating in which FCC phase is not present until a significant fraction is formed.
2. During austenitization in which BCC peaks are absent.

3. During cooling until reaching the *Ms* in BCC peaks are insignificant or absent.

As mentioned in section 2.4, there are four peaks of interest: $\{200\}_{FCC}$, $\{220\}_{FCC}$, $\{200\}_{BCC}$, and $\{220\}_{BCC}$. In the three temperature ranges described, properties of these peaks are wrongly identified. As the temperature rises, the BCC peak of {200} starts to disappear which indicates the start of a fully austenitic stage. Figure 16 shows that in the fully austenitic condition there is no detectable BCC peak, but there is a small peak in a lower 2θ position which may come from the minor phases like precipitates, carbides and oxides. The peaks which might correspond to minor phases like precipitates, carbides and oxides and which the intensity is in the order of background noise are called background peaks.

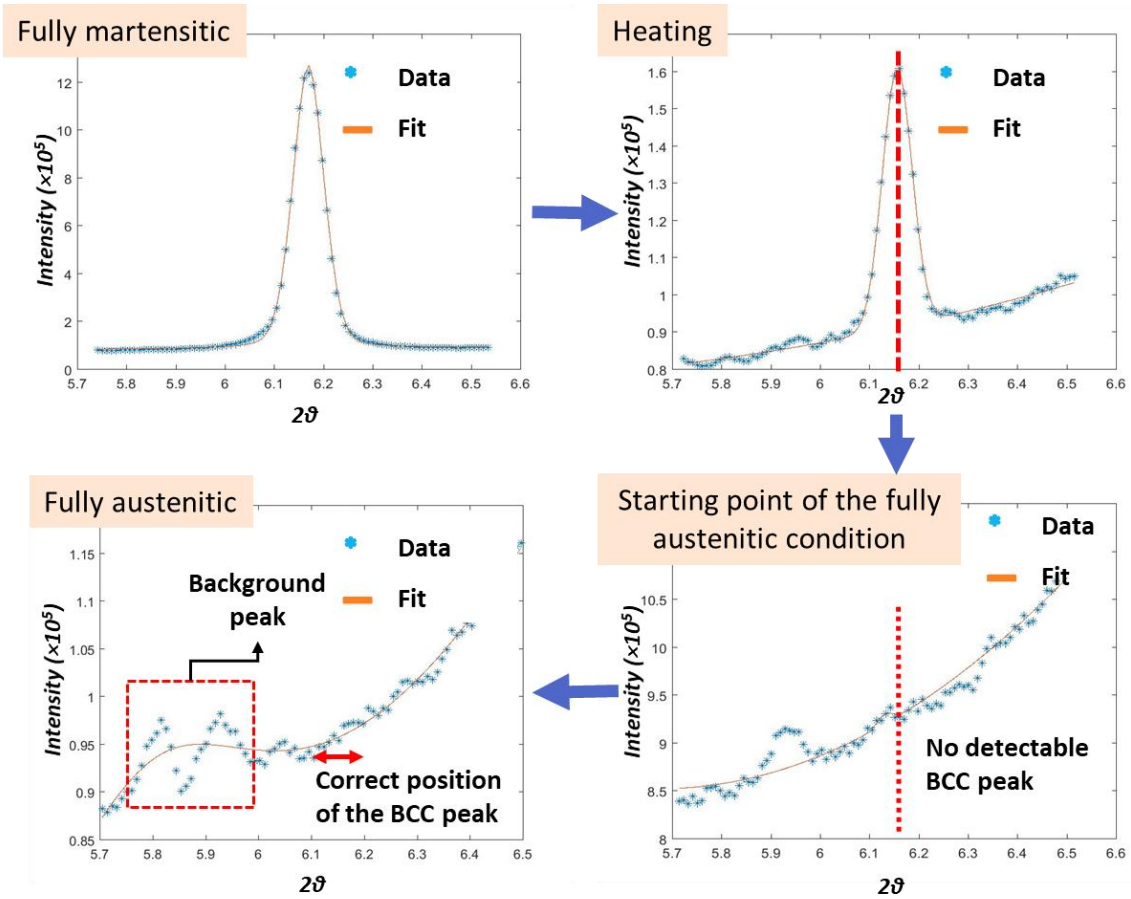

Figure 16 The fitting process performed by the fitting software. At first, the software correctly defined the peak properties of the BCC structure which is martensite. However, after the sample reached a fully austenitic condition, the software fitted the peak properties of the background peaks instead of ignoring the background peaks as done previously in the starting point of the fully austenitic condition.

Due to this error, the inaccuracy for calculating the phase fraction of the austenite at this particular temperature was equal to 0.10 of the austenite phase fraction. In this study, it was observed that the error due to the absence of the main phase (BCC or FCC) is found to vary between 10^{-3} to 0.10. The variation found was noted to correspond with the peak properties of the background peaks (peak intensity and peak area) and the number of background peaks

present. The illustration of the sensitivity of the program to the background spectrum is schematically shown in Figure 17. Based on the condition as mentioned above, therefore a manual inspection on each 1D spectrum is needed for finding the incorrect fitting. By doing so, incorrect data can be identified and subsequently, be ignored.

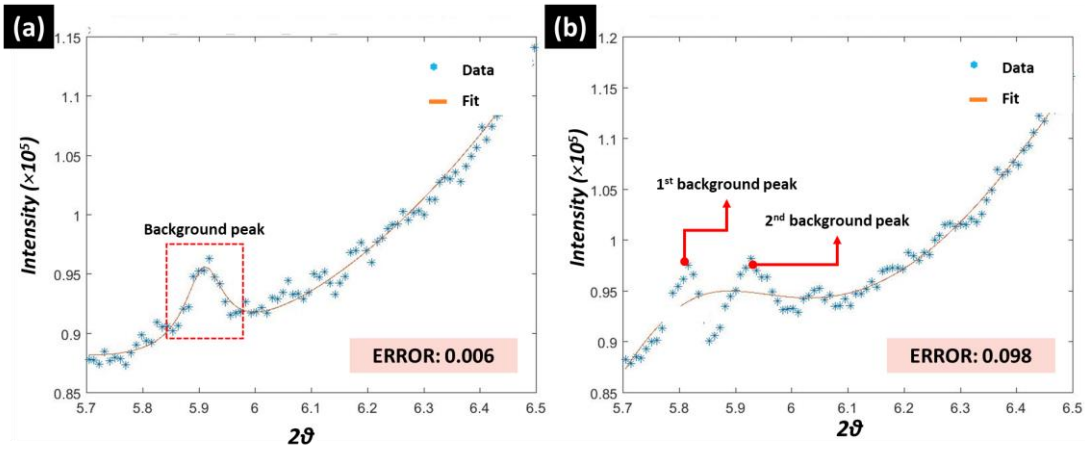

Figure 17 Two examples of the fitting process. These figures represent that the error in the calculation of phase fraction depends on the peak properties and the number of background peak present.

2.6.2 Peak Asymmetry

Finding peak properties is challenging when the peak is asymmetric. In this study, this asymmetry was observed in austenite peaks during the early stage of the bainite formation of the isothermal treatments performed at 350ºC and 305ºC. This asymmetric shape causes a scattering in the data of peak properties of the FCC such as the peak position.

However, the fluctuations found at the beginning of the isothermal treatments performed at 350ºC and 305ºC are not found at the tempering of the martensite. Thus, the fluctuations in austenite peak position observed in those two isothermal treatments are associated with the bainitic transformation. These fluctuations have been reported in several studies of bainite transformation [24], [25] and peak asymmetry is related to the presence of FCC austenite with an inhomogeneous carbon content [24].

An example of the asymmetric peak is shown in Figure 18 which displays the evolution of the peak shape of the FCC phase in the early stage of the isothermal treatment at 350ºC. The peak of {200} and {220} planes show slightly different shape over time, which can affect how the program fits the peak. This phenomenon causes fluctuations in the 2θ positions at the early stages of the mentioned isothermal treatments.

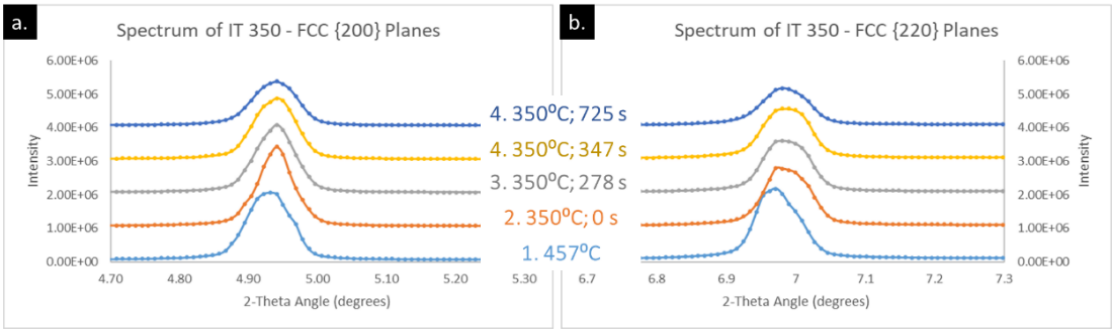

Figure 18 The evolution of peak shape in the FCC phase for a) {200} planes and b) {220} planes during isothermal treatment at 350°C.

Figure 19 shows the comparison between the peak position estimated by the fitting program and the experimental peak position. The general error for fitting the peak position by the program is measured to be ±0.01%. Using Equations (2-7) and (2-8), the error value can be translated into error in estimation of the carbon content which found to be ±0.01 wt.% C. In the study by Babu et al. [25], they tackled the error due to asymmetrical peak shape by separating the confounded peaks. However, in this study, the peak separation process was not implemented.

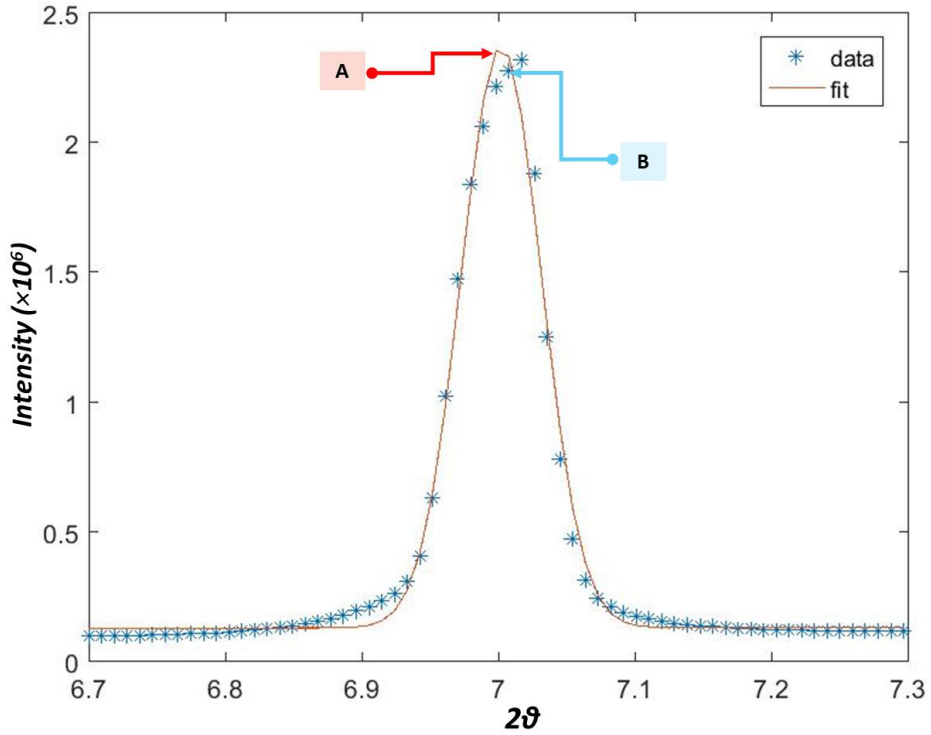

Figure 19 The result for the fitting of FCC $\{220\}_\gamma$ planes during isothermal treatment at 305°C. The figure shows a difference in the peak position obtained by the program indicated with point "A" and by manual (eye inspection) estimation indicated with point "B".

3

Results and Discussions

3.1 Heating Stage

The heating stage provides data for calculating the CTE of the martensite, as mentioned in section 2.5.3. In this study, each of the four heat treatments has its heating stage and, thus, CTE was calculated for each of them. These treatment-specific CTE were used in the analysis of thermal expansion for each treatment. The reason for using treatment-specific CTE instead of an average CTE from the four treatments is to reduce the error that may arise due to any slight difference between specimens. The results for the calculation of the experimental treatment-specific CTE are shown in Table 3. The CTE value between treatments is almost identical to each other which indicates that there is no major difference between the specimens used. Table 3 also shows that CTE of {200} planes have different value than CTE of {211} planes. It may be due to anisotropic strains experienced by martensite during the heating [52]. The CTE of the martensite presented in Table 3 is comparable to the CTE of martensite reported in several studies about microstructural evolution in low-C steel [52], [65].

Table 3 The treatment-specific CTE calculated for each martensite planes

Heating stage of the following treatment:	**CTE of α' (10^{-5} K^{-1})**	
	{200} BCC	**{211} BCC**
Direct quenching	1.52	1.44
Direct quenching followed by tempering	1.51	1.44
Isothermal treatment above *Ms*	1.52	1.43
Isothermal treatment below *Ms*	1.52	1.44

3.2 Rapid-Cooling Stage

Following heating and austenitization, all the studied four treatments underwent an initial rapid-cooling from the austenitization stage at 900°C to a given isothermal treatment temperature or to room temperature. Measurements corresponding to these four cooling stages provide information regarding the following three parameters: coefficient of thermal expansion of the austenite, *Ms* temperature and strains imposed by the martensite to the austenite.

3.2.1 Coefficient of thermal expansion (CTE) of the austenite

As mentioned in section 2.5.3, the rapid-cooling stage provides data for calculating the CTE of the austenite. The results for the calculation of the experimental treatment-specific CTE are shown in Table 4. These results are found to be comparable to the reported value of CTE of the austenite in the literature [64], [66].

Table 4 The treatment-specific CTE calculated for each austenite planes.

Cooling stage of the following treatment:	CTE of γ (10^{-5} K^{-1})	
	{200} FCC	{220} FCC
Direct quenching	2.23	2.32
Direct quenching followed by tempering	2.37	2.54
Isothermal treatment above *Ms*	2.68	2.56
Isothermal treatment below *Ms*	2.45	2.41

Compared to the CTE of the martensite, CTE of the austenite shows a larger variance between the treatments. The reason may come from the difference in temperature change rate used in the calculation of the CTE of the martensite and the austenite. As mentioned in section 2.2, the heating rate during the calculation of the CTE of martensite is slower (2°C/s) than the cooling rate (40°C/s) during the calculation of the CTE of the austenite. Therefore, the instruments may not be able to capture the data perfectly at a certain temperature as the sample may have undergone transformation for a lower temperature due to the rapid cooling rate.

3.2.2 Martensite start (*Ms*) temperature and the kinetics of martensite formation

As mentioned in section 2.4, the peak area of the SXRD calculated by the fitting software can provide the volume fraction of all the microstructures present in the steel sample. By assessing the evolution of the volume fraction of phases, the *Ms* temperature and the kinetics of martensite formation can be determined. Figure 20 shows the evolution of FCC-phase fraction on cooling from the austenitization conditions for all the studied heat treatments. A significant decrease in FCC-phase fraction occurring at a temperature of 319°C ± 8°C is observed, corresponding to the formation of a fraction of 0.05 martensite. This temperature is then identified as the experimental *Ms* temperature.

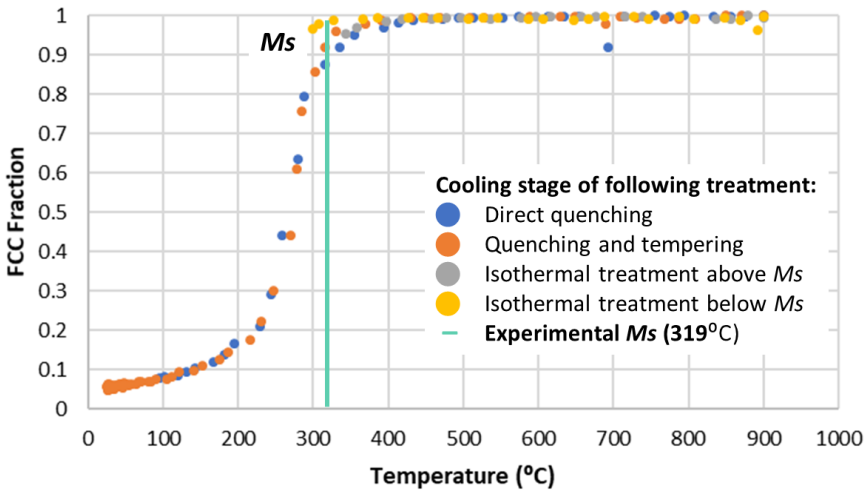

Figure 20 Evolution of FCC volume fraction during initial rapid-cooling in four of the treatments as a function of temperature.

The experimental *Ms* temperature measured by the SXRD is compared with the experimental value from the dilatometry experiment of the same material performed by Navarro-López et al. [35]. In the SXRD experiment, 319°C is the *Ms* temperature related to 0.05 phase fraction of the martensite. On the other hand, for the dilatometry experiment, 320°C is the *Ms* temperature related to 0.01 phase fraction of the martensite [35].

The difference in the results from the SXRD and the dilatometry mentioned before may come from the formation of the martensite at the surface. During rapid-cooling, it is expected that the surface of the sample is transformed first than the bulk of the sample. Based on literature [42], with only 1 mm^3 detection area, the formation of martensite at the surface may have a significant effect on the amount of martensite measured by the SXRD (high detected martensite fraction). However, for dilatometry, the formation of surface martensite may not affect much in the measurement. The surface may transform first into the martensite however there are other parts in the sample which significantly have a larger area than the surface that has not been transformed yet such as part which is located far from the heating elements of the dilatometry.

As mentioned earlier, the difference between measured martensite fraction in the SXRD and the dilatometry experiment is suspected due to the formation of surface martensite. In order to prove the formation of surface martensite, the corresponding diffraction patterns are studied further. Martensite is a microstructure formed by the displacive mechanism which occurred rapidly; thus the fast-growing rate can be linked with a sudden increase in the peak intensity of the BCC planes which directly related to the martensite fraction. During the rapid cooling stage, it was found that there were two formation rate ranges as schematically described in Figure 21. These two BCC formation rates measured during rapid cooling stage are higher than the formation rate measured during diffusional transformation, as happened during the heating stage. Therefore, the two fast formation rates of BCC structure found during rapid cooling may correspond to the displacive transformation which produces martensite. The first formation rate measured which is around 0.004 – 0.04 BCC fraction/s may correspond to the surface martensite. This formation rate of the surface martensite is found to be similar to that reported in the study by Villa et al. [52] (0.01 BCC fraction/s). From the same literature [52], the surface martensite is reported to form at higher temperatures than the expected *Ms* temperature. The second formation rate then exceeds 0.04 BCC fraction/s value at a temperature below the expected *Ms* temperature (319°C), therefore corresponds to a bigger volume of martensite which happened in the bulk of the steel sample. The finding of two martensite formation rates as observed in this study is in agreement with what is reported in the literature [52].

3.2.3 Strain imposed on the austenite during martensite formation

Figure 22 shows the evolution of the austenite lattice parameter during rapid-cooling in the temperature range around the *Ms* temperature. From this figure, it can be seen that the austenite lattice parameter starts to deviate from the theoretical thermal contraction value when martensite starts to form (below *Ms*). The formation of martensite initially induces compressive stresses until around 150°C, which corresponds to 0.89 volume fraction of martensite. As the temperature goes lower, the volume fraction of martensite keeps increasing which then is followed by a sharp increase in the austenite lattice deviation. This reversion of the stress state has been reported in several studies [52], [67], [68] and it indicates that the presence of martensite is affecting the lattice parameter of austenite.

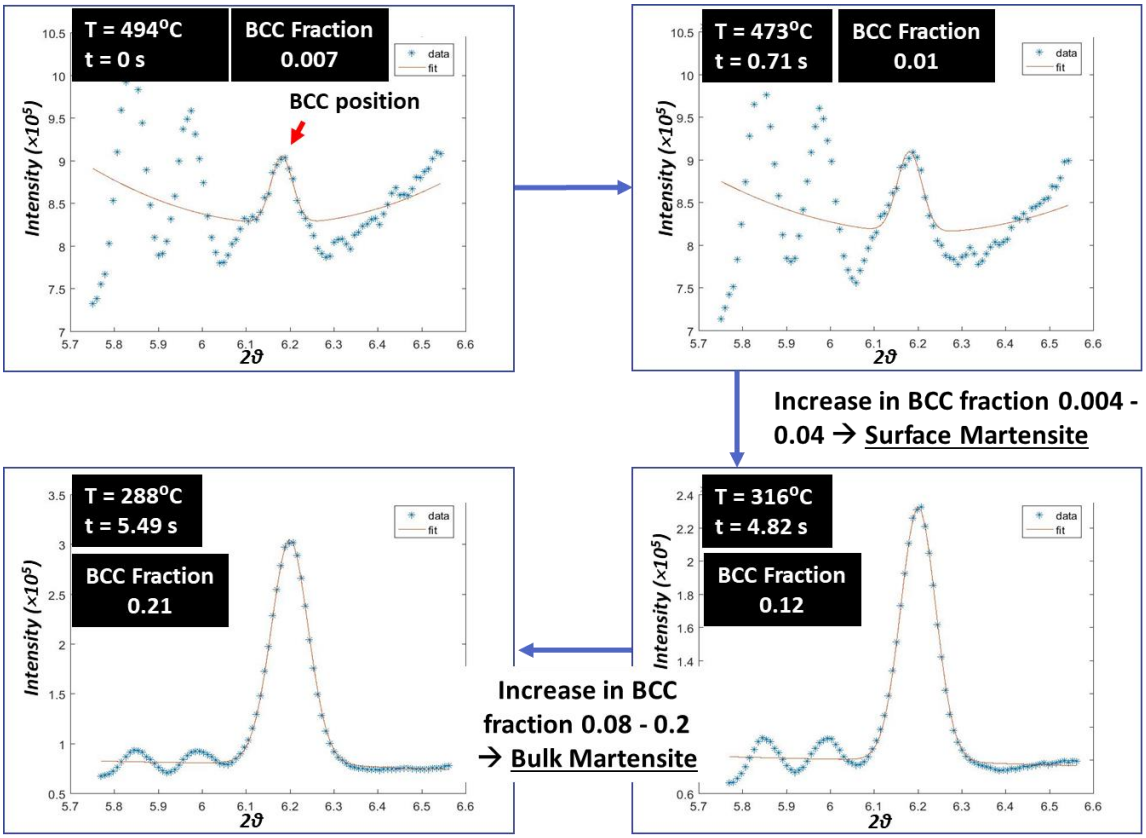

Figure 21 The growth of $\{200\}_\alpha$ in the sample over time during quenching. There are two martensite formation rates observed: the lower rate which happens at higher temperatures corresponds to the surface martensite and the formation rate for temperatures lower than the expected Ms temperature (319°C) is related to the bulk martensite. The x-axis of the graph is the peak position value (°) and the y-axis is the intensity (counts).

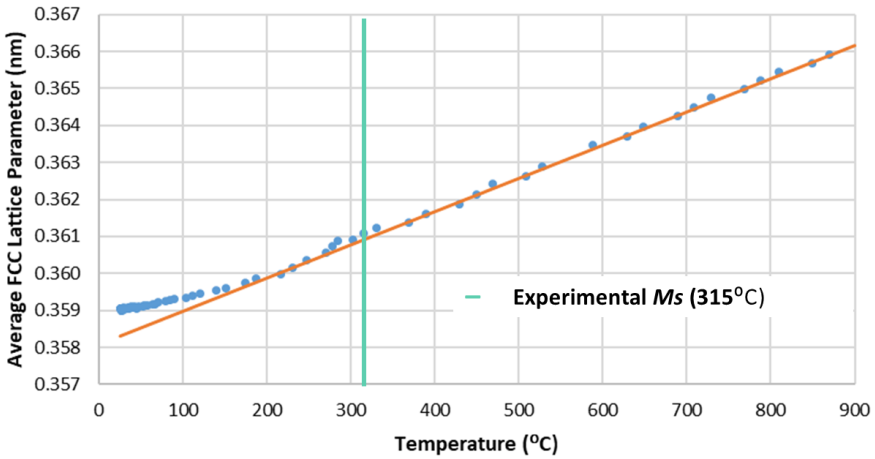

Figure 22 *The evolution of the average lattice parameter of austenite during the rapid-cooling stage as a function of temperature. The orange line represents the pure thermal contraction of austenite lattice parameter.*

At the end of the quenching stage of the direct quenching followed by tempering treatment, it was measured that there is 0.96 fraction of martensite present. The strains imposed on the austenite due to this martensite can be quantified. This strain experienced by the austenite is named strains contribution. The calculation of the strains contribution was performed by calculating the change between the theoretical and experimental value of FCC lattice $\left(\frac{a_{experimental}-a_{theoretical}}{a\ theoretical} = \varepsilon\right)$ and linking the strain (ε) with the corresponding BCC fraction. The calculation process is schematically described in Figure 23. Based on the function between martensite fraction and strains in the austenite lattice parameter shown in Figure 23, the presence of 0.96 martensite fraction at the beginning of the tempering treatment gives rise to strains equal to 0.002 and 0.001 for {200} planes and the {220} planes of austenite, respectively.

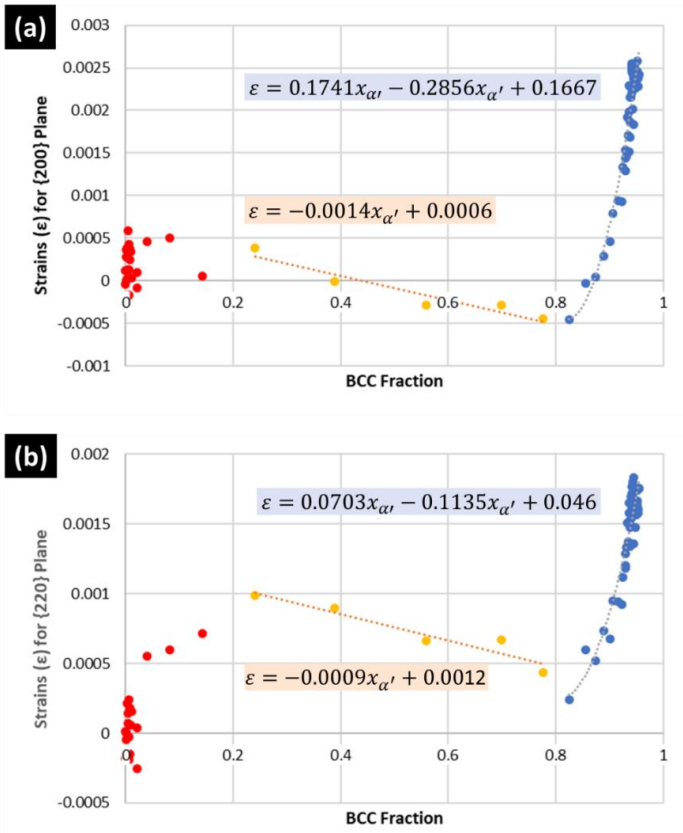

Figure 23 Relation between strains in the austenite lattice and BCC fraction fitted to a) {200} austenite planes and b) for {220} austenite planes in the quenching and tempering treatment. The red dots represent data points that are not used in the calculation due to its scattered nature. The yellow dots represent data points from 0.20-0.80 martensite fraction range while blue dots represent data points from martensite fraction larger than 0.80.

3.3 Analysis of the Quenching and Tempering (Q&T) Treatment

For quenching and tempering treatment, the detailed discussion on the quenching stage has been introduced in section 3.2. Therefore, the next sections are discussing the subsequent stages which are reheating and tempering stage.

3.3.1 Reheating Stage (from 25°C to 305°C)

The evolution of the lattice parameter of martensite and austenite during reheating is presented in Figure 24. In Figure 24(a), the measured lattice parameter of the martensite is represented by the green dot while the theoretical thermally expanded martensite lattice parameter is represented by the yellow line. Similar to it, for Figure 24(b), the measured austenite lattice parameter is symbolised with blue dot with the theoretical thermally expanded lattice parameter of the austenite is symbolised with orange lines. The grey line shown in Figure 24 is a theoretical thermally expanded austenite lattice parameter that has been added with the strains contribution calculated in section 3.2.3.

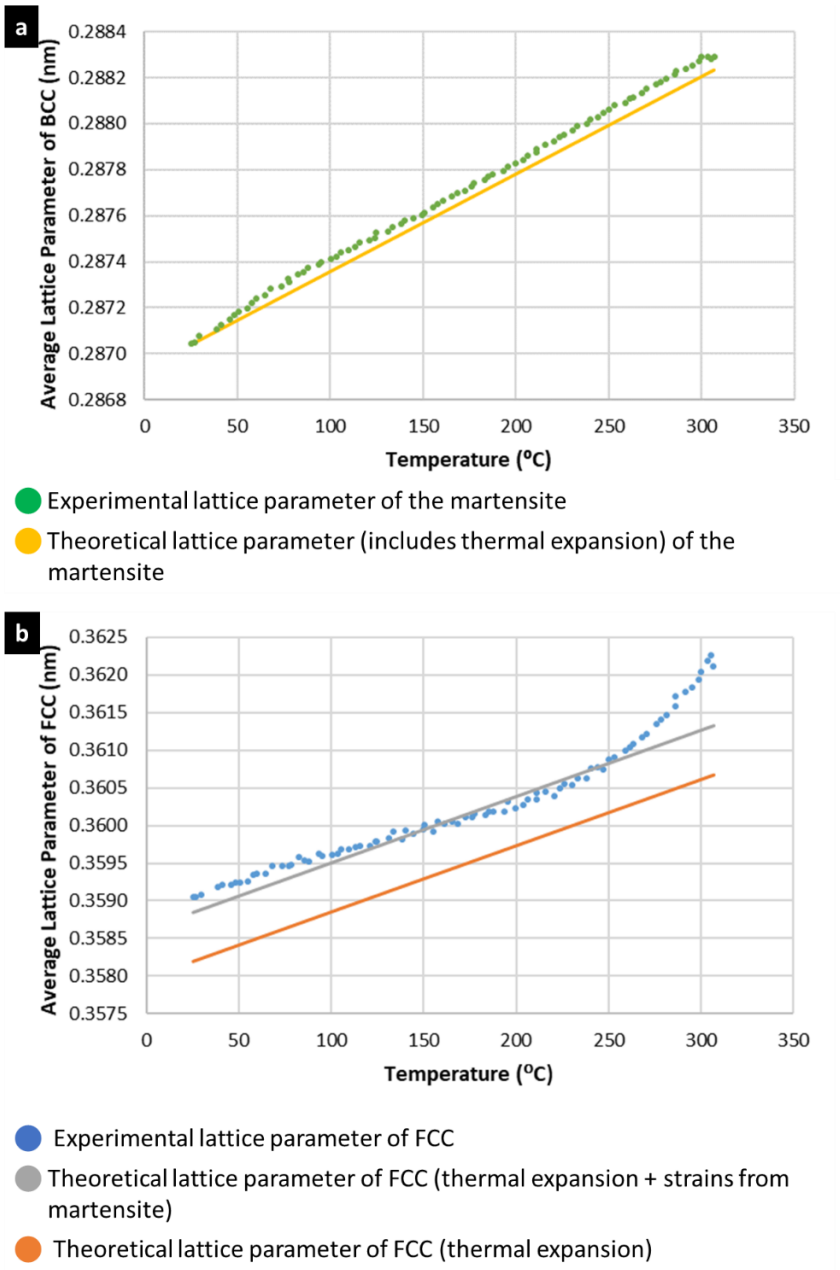

Figure 24 Evolution of the lattice parameter of a) martensite and b) austenite during reheating as a function of temperature.

Figure 24(a) shows that from room temperature to around 50°C, the rate of expansion of the measured martensite lattice parameter (green dots) is consistent with the theoretical thermally expanded martensite lattice parameter (orange line). From 50°C to 200°C, the measured martensite lattice parameter starts to deviate further with an increase in lattice difference from 50°C to 100°C, followed by a very slow increase.

The finding of three different behaviours in the evolution of the martensite and the austenite lattice parameters has been reported by Villa et al. [52]. The three stages observed by Villa et al. [52] may also be occurring in the present study. The details of each three stages are as follow:

1. At temperature range between room temperature and 50°C, the consistency between measured lattice parameter of the martensite and theoretical thermally-expanded lattice parameter of the martensite shows that in this range only thermal expansion of the martensite occurred.
2. At temperature range from 50°C to 200°C, the deviation of both martensite lattice parameter shown in Figure 24(a) and austenite lattice parameter shown in Figure 24(b) shows that the process occurred is not only the thermal expansion of both martensite and austenite but also stress relaxation of the austenite.
3. At the end of the reheating stage, it can be seen, especially from Figure 24(b), that the lattice parameters of the crystal structures start to give a significant deviation from the theoretical value. Comparing the deviation at this temperature range with the deviation at temperature range from 50°C to 200°C, the deviation in the latest temperature range is larger. Therefore, in addition to stress relief process of the austenite, another process that increases the austenite lattice parameter occurs which in this study may be related to the carbon redistribution process from the martensite to the austenite as also reported by Villa et al. [52].

The comparison between the temperature ranges reported in the literature with its corresponding phenomenon behind it and the temperatures ranges observed in this study are presented in Table 5.

Table 5 Comparison between three observed temperatures ranges during reheating from the literature [52] *and the experiments performed in this study.*

No.	Temperature Ranges		Phenomenon
	Reported by Villa et al. [52]	**Experimental Temperature Ranges**	
1	< 150°C	Room temperature - 50°C	Only thermal expansion (TE)
2	150°C - 475°C	50°C - 200°C	TE + partial stress relief of the austenite
3	475°C - 625°C	>200°C	TE + carbon redistribution process from the martensite

3.3.2 Tempering Stage (305°C)

Subsequent to reheating, the sample was then isothermally treated at the temperature of 305°C. The evolution of lattice parameter and phase fractions of austenite (FCC) and martensite (BCC) are presented in Figure 25. Figure 25(a) shows that the phase fractions of both FCC and BCC do not significantly change during tempering, which indicates that there is no phase transformation during this process. The BCC fraction has a constant value over the treatment which is 0.96.

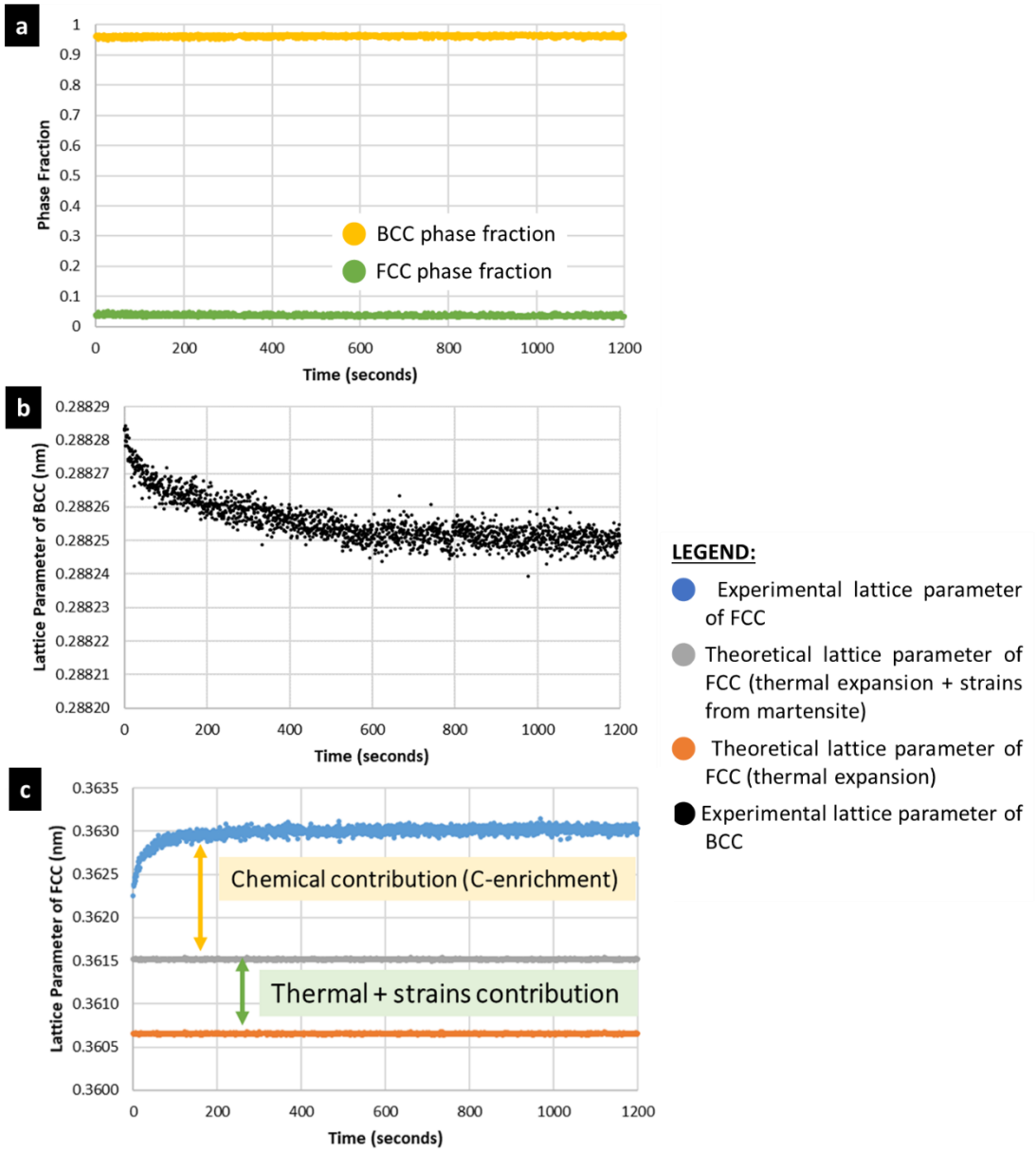

Figure 25 The evolution of the lattice parameter of the a) martensite and b) the austenite during tempering as a function of temperature

The evolution of lattice parameter of BCC during tempering exhibits a steady decrease in the first 400 seconds of tempering before reaching a constant value, as depicted in Figure 25(b), which is related to the diffusion of the carbon atoms out of the supersaturated martensite. These carbon atoms may partition into the austenite as well as segregate into lattice defects or precipitate as carbides [31], [69].

The carbon partitioning from martensite into the austenite can also be observed from the change in the austenite lattice parameter. As shown in Figure 25(c), the observed increase in FCC lattice during the first 120 seconds is probably a consequence of the partitioning of carbon from martensite into adjacent austenite during tempering of martensite [69], [70]. Thomas et al. [69] reported that the tempering at 400^{o}C of a 0.31 wt.% C martensitic sample with 0.10 volume fraction of retained austenite resulted in an evolution of the austenite lattice parameter which started with a significant expansion in the first 30 seconds, followed by a constant value. The behaviour of the austenite lattice parameter evolution observed in this study is comparable.

The segregation of carbon atoms and the carbide precipitation cannot be directly detected via SXRD since the number of carbon atoms which are segregated or precipitated are significantly lower compared to the carbon atoms contained in the major phase such as austenite [69]. However, as shown in Figure 25(b), the lattice parameter of martensite continues to decrease even after 120 seconds in which the austenite lattice parameter has reached its maximum value. Therefore, it can be concluded that the carbon atoms from the martensite segregate into dislocations which usually are found in low-C steels [31], or they may form carbides [69].

By subtracting the thermal and strain contributions, the change in austenite lattice during tempering due to carbon partitioning can be calculated, as schematically shown in Figure 25(c). Applying Equation (2-7) to the lattice parameter of the austenite at the beginning and the end of tempering, the estimation of C-enrichment in the austenite is calculated. At the beginning of tempering, the retained austenite contains 0.22 ± 0.01 wt.% C and after tempering for 1200 seconds, the C-content increases to 0.45 ± 0.01 wt.% C. The study by Thomas et al. [69] reported that for 0.31C steel tempered at 400^{o}C for 1000 seconds, the carbon content in the austenite changed from 0.31 wt.% C to 0.60 which is a change comparable to the one observed in the present work. Applying Equation (2-8) to the martensite lattice parameter at the beginning and the end of the tempering treatment results in the change of carbon content in the martensite from 0.14 ± 0.01 wt.% C to 0.13 ± 0.01 wt.% which correspond to martensite phase fraction 0.960 and 0.958. Assuming that the total carbon content in the sample is equal to the bulk carbon concentration of the steel (0.2 wt.%) then it was found that there is 0.005±0.01 wt.% C that is neither in austenite nor martensite which in this case represent the carbon atoms that precipitate or segregate.

3.4 Analysis of the Isothermal Treatment at 350^{o}C (above *Ms*)

The isothermal treatment above *Ms* was designed to study bainite formation. Prior to the isothermal treatment, the sample was rapidly cooled from the austenitization condition at 900^{o}C to 350^{o}C. During this cooling stage, as observed in Figure 26, the amount of BCC fraction starts to increase at a temperature lower than the theoretical *Bs* temperature written in Table 2 (397ºC). In order to prove that this BCC structure measured here is bainite instead of martensite, further investigations on the evolution of the BCC phase fraction was carried out. By comparing

the increasing rate of the BCC fraction found in this stage with the increasing rate of the BCC fraction for the martensite formation mentioned in section 3.2.2, the BCC formation rate value measured during this cooling stage is smaller (0.002 BCC fraction/s). Therefore, it can be concluded that the 0.05 fraction of BCC detected at the end of the rapid-cooling stage (or the beginning of the isothermal treatment stage) is bainite instead of martensite.

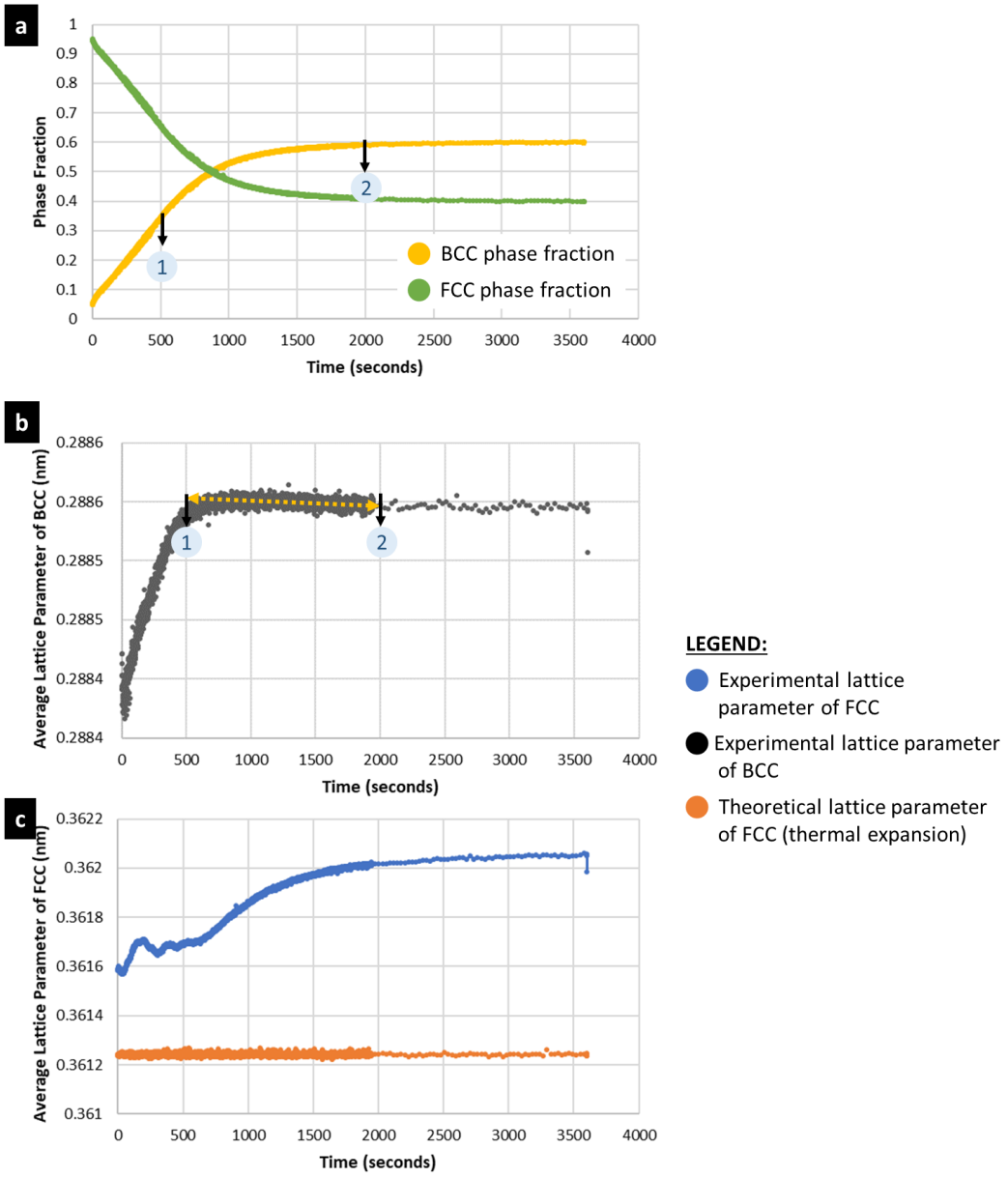

Figure 26 a) The evolution of phase fractions and the evolution of lattice parameter of the b) bainite and c) austenite during isothermal treatment above Ms as a function of time.

Figure 26 presents the evolution of the lattice parameters and phase fractions of the BCC and FCC structures during this isothermal treatment. Figure 26(a) shows that the BCC fraction increases during the first 1500 seconds of the treatment before reaching a constant value, indicating the formation of bainite. Figure 26(a) shows a decreasing of the FCC fraction in the

same time range. After 2000 seconds of isothermal treatment, both phase fractions of austenite and bainite have reached a constant value, which indicates that bainite formation has ceased.

The bainite formation is observed to cause an increase in the lattice parameter of BCC at the first 500 seconds of the treatment, as shown in Figure 26(b). The increase comes from the initiation of bainite formation in the low carbon region of austenite, where austenite is more prone to be transformed into bainitic ferrite as reported by Babu et al. [25]. Bainite forming in regions with lower carbon content will also contain lower carbon than bainite formed at later stages. This condition explains the increase in the lattice parameter corresponding to BCC bainite during the isothermal treatment.

The increase in BCC lattice parameter stops as the isothermal treatment reaches 500 seconds, which corresponds to around 0.40 of BCC fraction (point 1 in Figure 26(b)). A small decrease in BCC lattice is then observed until a fraction of BCC of around 0.60 is reached (point 2 in Figure 26 (b)), which may be consequence of further carbon partitioning from the bainitic ferrite to the austenite, carbides precipitation or carbon segregation into defects, which can also be found during bainite formation [18]. However, in this time range (500 s – 2000 s) bainitic ferrite still grows, as shown in Figure 26 (a). Therefore, in this time range, the processes that are happening are coupling processes between the decrease in the lattice parameter of the initially formed bainite due to carbon redistribution processes and the increase in the lattice parameter of the newly formed bainite due to its formation from carbon enriched austenite. This behaviour is similar to that observed in a study by Timokhina et al. [24].

In the final stage of the isothermal treatment, the BCC lattice parameter reaches a plateau, indicating that all the bainite formed has reached its equilibrium controlled by its T_0' curve. This behaviour is comparable to what is reported in the literature [15], [49], [71].

In addition to the evolution of BCC lattice parameter, Figure 26 also shows the evolution of FCC lattice parameter during the isothermal treatment above *Ms*. From Figure 26(c), it can be seen that, during first 600 seconds of the treatment, there are fluctuations in the value of austenite lattice. This condition is a result of the asymmetrical peak shape found in the corresponding diffraction patterns, which can cause poor peak fitting, as mentioned in section 2.6.2. Based on the literature [24], [49], the asymmetrical peak shape is due to the inhomogeneous carbon concentration in the austenite grains at the initial stages of bainite formation. The simultaneous C-partitioning from bainite and the growth of bainite leads to the formation of C-enriched austenite regions near sub-units of bainite and C-poor austenite regions far from the bainite.

Similar to martensite, strains are also developed during the transformation from austenite to bainite [72]. However, different from martensite, the strains imposed by bainite to the austenite are more challenging to be evaluated. The growth of bainite in parallel with carbon partitioning to adjacent austenite makes the separation between strain and chemical contributions difficult. Therefore, in this study, the strains imposed on the austenite due to bainite formation are not considered further.

Excluding the strains imposed by the bainite to the austenite, the difference between theoretical thermally expanded austenite lattice parameter values and experimental austenite lattice parameter values during the isothermal treatment can be regarded as a result of carbon partitioning from the bainite to the austenite.

Applying Equation (2-7) in the difference between the thermally expanded lattice and experimental austenite lattice parameter at the beginning of the isothermal treatment approximates that the austenite contains 0.10±0.01 wt.% C. At the same time, applying Equation (2-8) to the lattice parameter of bainite at the beginning the treatment shows that the carbon content in the bainite is equal to 0.12 ± 0.01 wt.% C. Based on these calculations, the total carbon from austenite and bainite at the beginning of the treatment is equal to 0.11 ± 0.01 wt.% C which is lower than the C-content of the bulk (0.2 wt.% C). The difference may be caused by the underestimation of the peak position of the austenite which can be translated into the underestimation of the C-content of the austenite. The underestimation in the peak position of the austenite is due to the formation of asymmetrical shape as mentioned in section 2.6.2.

At the end of the treatment, applying Equation (2-7) and (2-8) to the lattice parameter of austenite and bainite at the end of the treatment, results in the C-content of the austenite is equal to 0.23 ± 0.01 wt.% C and bainite is equal to 0.15 ± 0.01 wt.% C. Assuming that the total carbon in the sample is equal to the bulk content of the steel (0.20 wt.%) then it is found that there is around 0.02 ± 0.01 wt.% of carbon which is not contained in either austenite or bainite. At the end of the treatment, the austenite peaks do not show asymmetrical feature. Thus, the difference in the C-content observed here is not due to the underestimation of the austenite peak position. The reason may come from the carbon which segregates in the dislocations or precipitates as carbides [15], [49], [71]. At the end of the treatment, the increase in the C-content of the austenite from 0.10 wt.% C to 0.23 wt.% C is expected due to the enrichment from the bainite.

3.5 Analysis of the Isothermal Treatment at 305°C (below *Ms*)

The focus in this study is to investigate the processes that occur during isothermal treatments below *Ms*. Before the sample is isothermally treated at 305°C, it was rapidly cooled to this temperature from 900°C. In this cooling stage, there is a sudden increase in BCC fraction after 327°C, as shown in Figure 27, which indicates the formation of martensite. Reaching 305°C, the volume fraction of martensite formed is 0.034. Based on the dilatometry experiment on the same material [35], for isothermal treatments at a temperature between 300°C and 310°C, the amount of the martensite present should be between 0.04 and 0.16 which is higher than measured in this study (0.034).

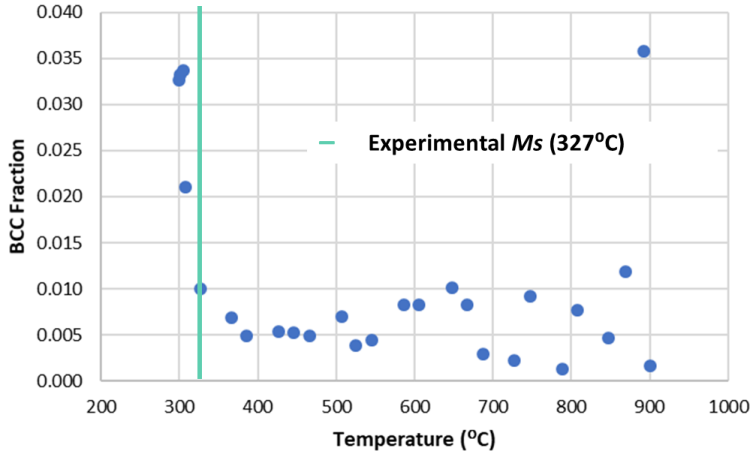

Figure 27 The evolution of BCC fraction as a function of temperature during rapid cooling before isothermal treatment at 305°C.

Two reasons may cause the difference in the volume fraction of martensite measured smaller than expected from the dilatometry experiments [35] which are:

1. There may be an instrumental error, i.e. error in the thermocouple, during the in-situ SXRD experiments, leading to the measurement of a temperature lower than the real temperature in the material, which led to a fraction of martensite lower than expected.
2. There might be a slight difference in the chemical composition of the steel used in the isothermal treatment below *Ms* and the steels used in the other three treatments in this work. Figure 28 shows that at the temperature range 300°C - 400°C, the formation kinetics of BCC measured in the case of the isothermal treatment below *Ms* is slightly delayed than in the other three treatments. A slight difference in chemical composition might explain this effect.

However, the offset between the current experiment and dilatometry experiment [35] is not expected to affect much of the results. It is because the temperature range (310°C – 320°C) suggested by the dilatometry for 0.03 BCC phase fraction as measured in this study, is still lower than the expected *Ms* temperature presented in Table 2. Therefore, the objective to achieve treatment temperature below *Ms* is not compromised.

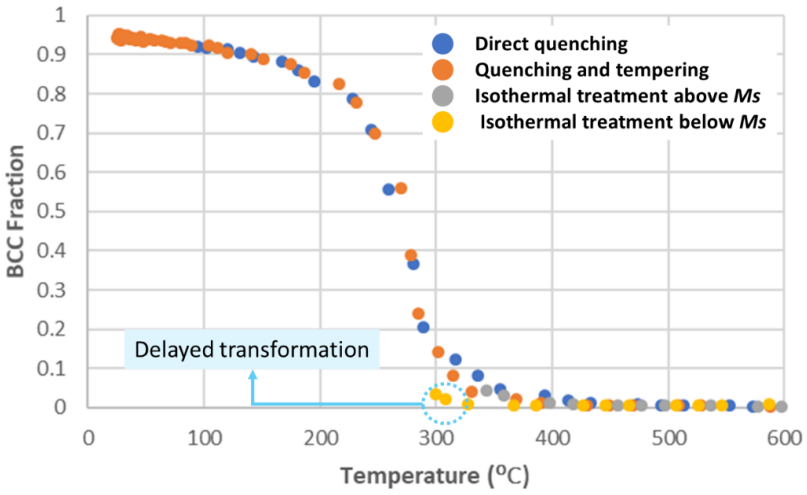

Figure 28 The evolution of BCC fraction during rapid cooling of all the four treatments.

The evolution of the lattice parameter of the austenite (FCC) shown in Figure 29(a) indicates fluctuations in the first 400 seconds of the isothermal treatment, which corresponds to the formation of a bainite fraction equal to ± 0.28. The fluctuations are then followed by an increase in the lattice parameter of austenite until around 3500 seconds before it becomes constant. As discussed in section 2.6.2, the fluctuations observed indicate an inhomogeneous carbon concentration in the austenite. Moreover, bainite is formed right after the isothermal treatment started which was also obtained in dilatometry experiment [35]. The formation of bainite is also supported by the decrease in the phase fraction of FCC, as presented in Figure 29(b).

The increase in the austenite lattice parameter after 400 seconds is followed by a constant value, behaviour that was also observed during the isothermal treatment above *Ms*. In that case, the evolution of the austenite lattice parameter was a consequence of carbon diffusion out of the

bainite subunits during bainite formation, as discussed in section 3.4. However, in the case of treatment below *Ms*, carbon atoms may come from both prior athermal martensite and bainite. As the amount of prior athermal martensite is relatively small compare to bainite, its contribution to the carbon enrichment of the austenite may be smaller than that of the bainite. The constant value of the austenite lattice parameter at the end of the treatment is related to the completion of the bainite formation.

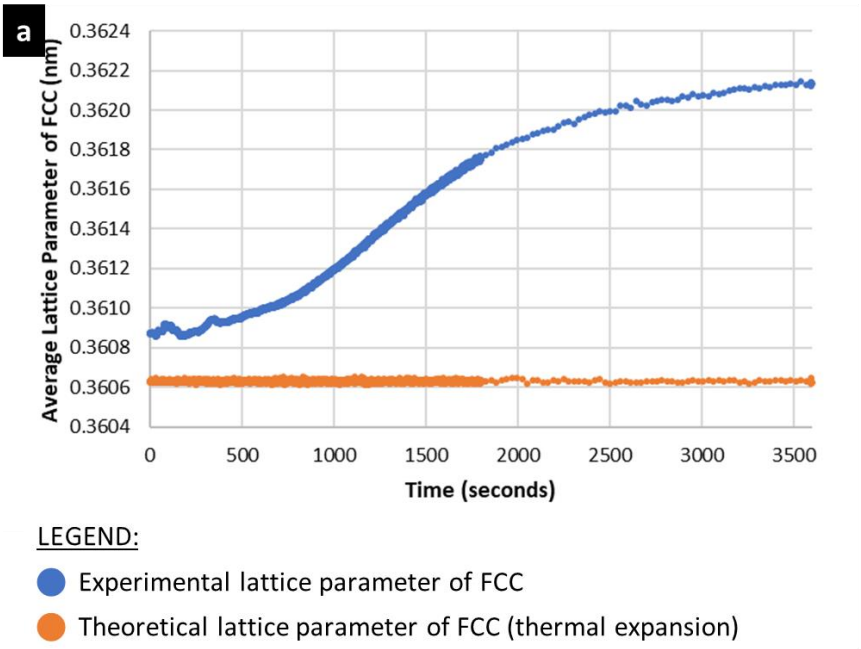

Figure 29 The evolution of lattice parameter of a) FCC phase and b) FCC phase fraction at the isothermal treatment 578K as a function of time.

The evolution of the BCC lattice parameter is presented in Figure 30(a), showing that in the first 500 seconds, the BCC lattice parameter value decreases rapidly, coinciding with fluctuations in the austenite lattice which corresponds to the formation of bainite [24], [25]. This feature is then

followed by a slower decrease in treatment time between 500 – 1500 seconds and ending up with a constant lattice parameter value from 1500 seconds onwards.

However, in the isothermal treatment above *Ms* (section 3.4), the formation of bainite is accompanied by an increase of the BCC lattice parameter. In that case, the only BCC structure present in the specimen is bainite, while in the present case, the microstructure after the decrease in the first 500 seconds of the BCC lattice parameter is a mixture of around 0.034 volume fraction of martensite and around 0.4 volume fraction of bainite.

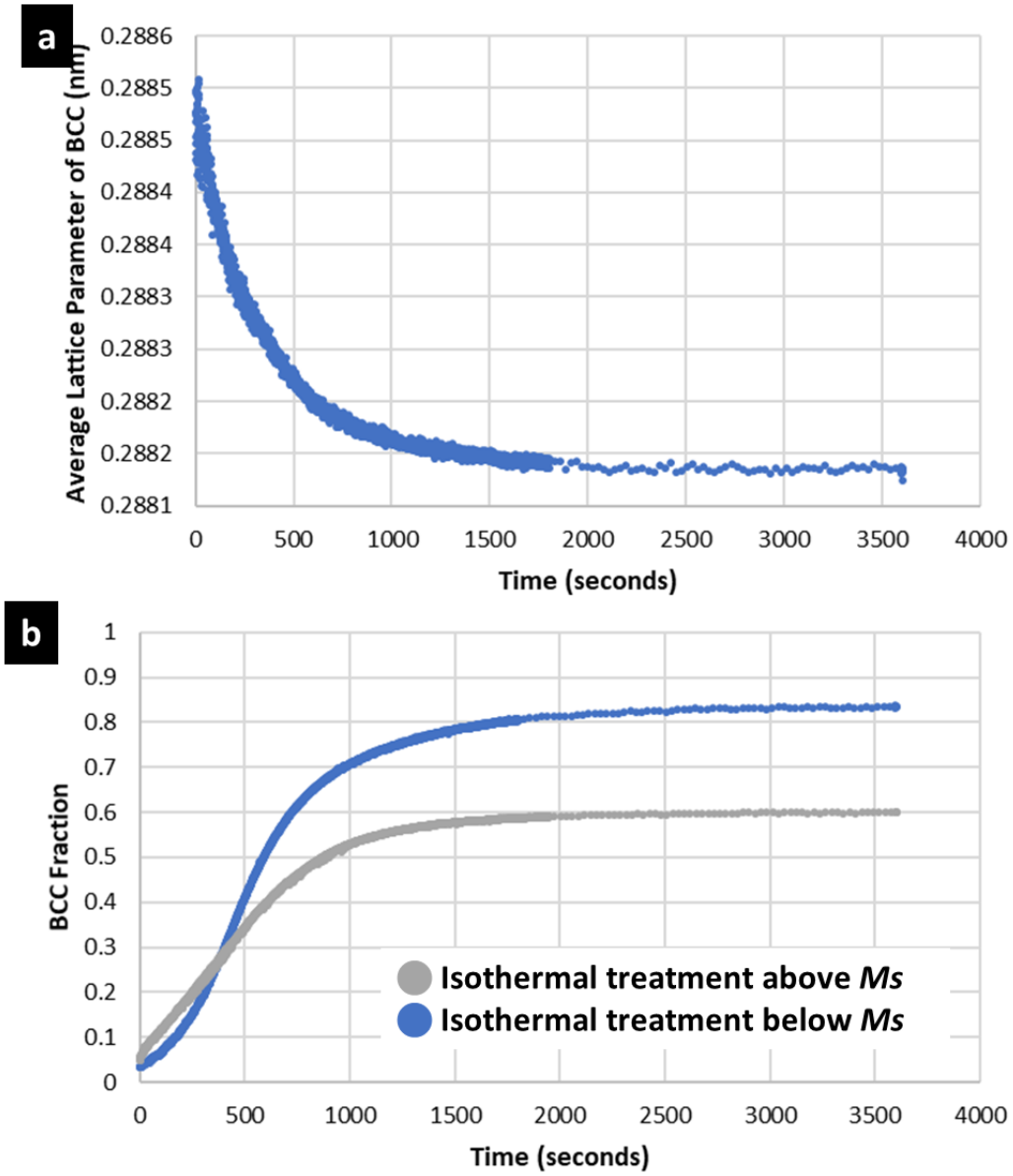

Figure 30 The evolution of a) BCC lattice parameter as a function of time and b) a graph shows the comparison in the evolution of the BCC phase fraction of the two isothermal treatment above and below Ms as a function of time.

Prior to the isothermal treatment below *Ms*, the BCC structure present in the steel was martensite. As the product of displacive transformation, martensite contains similar carbon content to the parent austenite. Applying equation (2-8) to martensite lattice parameter at the beginning (t = 0 s) of the isothermal treatment below *Ms* results in C-content of the martensite id equal to 0.20 ± 0.01 wt.% C. As the isothermal treatment below *Ms* proceeds, bainite starts to form, probably from the low-C content austenite (as discussed in section 3.4). The formation of bainite leads to a reduction of the average BCC lattice parameter measured by the SXRD, as bainite has a smaller lattice parameter than the initially detected BCC structure which is martensite. Carbon redistribution processes from bainite through the partition to the adjacent austenite, carbon segregation, or carbide precipitation may also contribute to the fast decrease in the first 500 seconds.

Based on Figure 30(a), a continued decrease of the BCC lattice parameter from 500 seconds until 2000 seconds may correspond to the continuation of the growth of the bainite. The growth of the bainite is then stopped as indicated with a constant value of the BCC lattice parameter after 2000 seconds. However, carbon enrichment of the austenite is suspected still to occur as the austenite lattice parameter still shows an increase even after 2000 seconds, as shown in Figure 29(a).

Applying Equation (2-7) and Equation (2-8) to the lattice parameter of austenite and martensite present at the beginning of the isothermal treatment below *Ms*, results in the C-content of the austenite and martensite are equal to 0.07±0.01 wt.% C and 0.20 ± 0.01 wt.% C respectively. Comparing the total carbon of the austenite and martensite present here and the C-content of the bulk sample, the calculated value is much lower. It may be due to the formation of the asymmetrical peak of the austenite (section 2.6.2) which later causing an underestimation in the calculation of the C-content of austenite.

At the end of the isothermal treatment, the C-content of austenite changes from 0.07±0.01 wt.% C to 0.45 ± 0.01 wt.% C. Comparing to the C-enrichment of the austenite during isothermal treatment above *Ms* which is changed from 0.10±0.01 to 0.23+±0.01 wt.% C, the value of the C-enrichment in the isothermal treatment below *Ms* is higher. This is expected with the decrease of the temperature since the solubility of carbon in the austenite that is in equilibrium with ferrite increases [73].

In addition to that, as there is no formation of asymmetrical peak of austenite, calculating the fraction of carbon in the BCC constituents through Equation (2-8) and considering the fraction of carbon in the austenite through Equation (2-7), results show that there is 0.05 ± 0.01 wt.% C at the end of the treatment that is not located in either BCC structures or FCC structures. The value represents carbon redistributed in dislocation or precipitated as carbides. Comparing with the isothermal treatment above *Ms*, the number of carbon atoms which are segregated or precipitated is higher in the isothermal treatment below *Ms*. One of the reasons may come from the presence of martensite which introduced additional dislocation into the steel. Thus, providing additional sites for carbon segregation. With a lower treatment temperature, the carbon movement becomes slower than in isothermal treatment above *Ms*. Therefore, it may be easier for the carbon atoms to segregate in the dislocation lines attached to the martensite formation than to diffuse into the austenite.

In Figure 30(b), after 500 seconds, in the same time period, the amount of bainite formed at the isothermal treatment below *Ms* is higher compared to the isothermal treatment above *Ms*. In order to get clearer comparison, calculation of the nucleation rate and density of potential nucleation sites, assuming that the bainite grows without diffusion of carbon [35] is then performed. The change in bainite fraction (f^B) as a function of time (t) can be described as [35]

$$\frac{f^B}{dt} = \frac{dN}{dt} . V_0 \left(\frac{T - 528\ K}{150\ K} \right) \tag{3-1}$$

with dN/dt is the nucleation rate per unit of volume ($m^{-3}s^{-1}$), V_0 is the constant related to the initial volume of bainite which is equal to $2 \times 10^{-17}\ m^3$, and T is the isothermal holding temperature measured in Kelvin. The difference in the nucleation rate of the isothermal treatment above and below *Ms* based on Equation (3-1) can be observed in Figure 31.

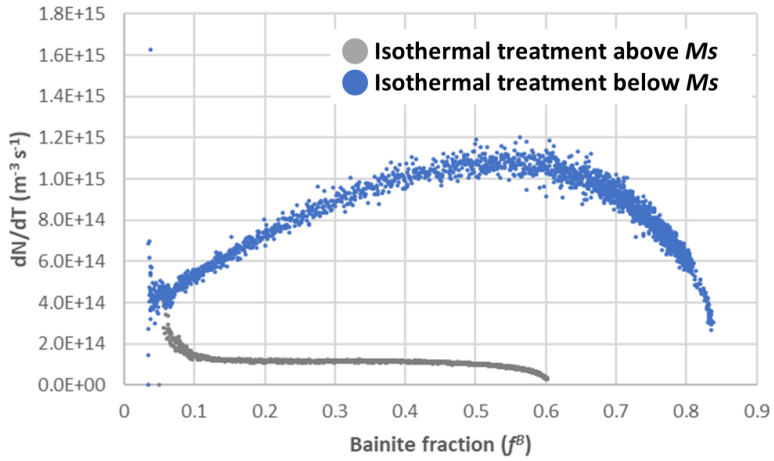

Figure 31 Evolution of nucleation rates of isothermal treatment below and above Ms.

Figure 32 shows that initially (for bainite fraction below 0.1), the nucleation rate of bainite between isothermal treatment above and below *Ms* is similar which is also shown in Figure 30(b). For the isothermal treatment above *Ms*, the nucleation rates decrease and reach a constant value of nucleation rate between 0.1 – 0.5 fraction of bainite before decrease again until reach its maximum bainite fraction. The range where the nucleation rate shows a constant value coincides with the constant increase in bainite formation at isothermal treatment above *Ms* as shown in Figure 30(b).

On the other hand, the kinetics for isothermal treatment below *Ms*, the nucleation rates keep increasing until reach a maximum at bainite fraction between 0.5 and 0.6. These bainite fraction values coincides with the turning point between increase in kinetics and gradual decrease region of the bainite formation at the isothermal treatment described in Figure 30(b). The low isothermal temperature contributes to the increase in the undercooling. Thus, the driving force for nucleation increases and results in the faster transformation observed in the isothermal treatment below *Ms*.

The difference in the characteristics of the evolution of nucleation rate between isothermal treatment above and below *Ms* may also related to the presence of the martensite prior to the isothermal treatment below *Ms* which do not form at the isothermal treatment above *Ms*. The presence of martensite results in the formation of martensite/austenite interfaces which can act

as potential nucleation sites for bainite. This phenomenon is supported with the SEM observations of the same material performed by Navarro-López et al. [21]. It showed that some of the bainitic ferrites have a similar crystallographic orientation relationship with the prior athermal martensite. Therefore, it was suggested that these particular bainitic ferrites grow from the prior athermal martensite.

Based on the aforementioned processes, the microstructural developments occurred in the isothermal treatment below *Ms* are schematically described in Figure 32.

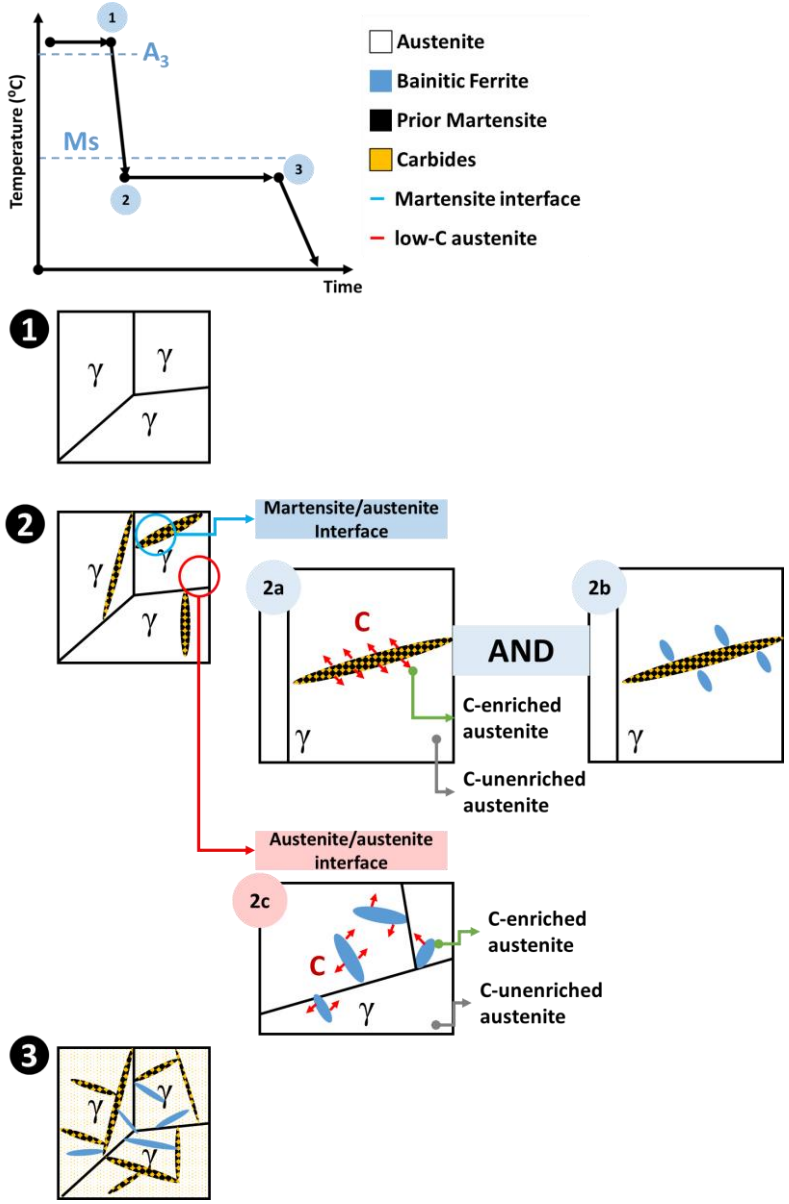

Figure 32 The schematic of the process occurred during isothermal treatment below Ms. 1) A fully austenitic condition, 2) Formation of martensite upon rapid-cooling, 2a) C-redistribution processes from the martensite, 2b) formation of bainite at the martensite/austenite interface, 2c) simultaneous processes of bainite formation and C-redistribution processes from the bainite, 3) Final condition which consists of martensite, bainite, and C-enriched austenite.

The microstructural developments illustrated in Figure 32 are based on the observed features in the evolution of lattice parameter and phase fraction of BCC and FCC structures. The microstructural evolution below *Ms* is suggested to occur as follows:

1. Rapidly cooled sample from austenitization temperature to isothermal treatment below *Ms* (305°C) leads to the formation of martensite. The martensite formation is supported by a sharp increase in the BCC phase fraction measured by the SXRD.

2. During isothermal holding, four processes occur simultaneously:
   a. Carbon redistribution from the athermal martensite through C-partition to the adjacent austenite, C-segregation, and carbide precipitation. In addition to the carbon balance calculated from the austenite and BCC structures (martensite/bainite) obtained from the diffractograms, the formation of carbides from athermal martensite is supported with SEM micrographs [21]. The micrographs showed that there are carbides visible within the microstructural features which have martensitic nature.
   b. Formation of bainite from the martensite/austenite interfaces.
   c. Formation of bainite from the austenite/austenite interfaces. As mentioned in section 3.4, without the presence of martensite, bainite is suggested to form from the low-C austenite region (austenite/austenite interface).
   d. Carbon redistribution processes through C-partition to the adjacent austenite, C-segregation, and carbide precipitation from bainite. Different with C-redistribution processes from the martensite, carbide precipitation is more unlikely to happen in the C-redistribution processes from bainite. The reason is that from the SEM observations [21], there are no carbides visible within the microstructural features identified with bainitic nature.

3.6 Final Quenching Stage of All the Treatments

Following isothermal treatments around *Ms*, all the studied three treatments: tempering, isothermal treatment above *Ms*, and isothermal treatment below *Ms*, underwent final quenching from a given isothermal treatment temperature to room temperature. The data obtained during this final quenching stage is then used to study the stability of the austenite that has been enriched with carbon during isothermal treatment around *Ms* temperature.

As mentioned in section 3.3.2, 3.4, 3.5, during the three isothermal treatments, the BCC structures enrich the austenite with their carbon atoms. The carbon enrichment of the austenite leads to lower *Ms* temperature of the steel. If the carbon enrichment is such that the *Ms* characteristic of the austenite falls below room temperature, austenite becomes retained at room temperature. The presence of retained austenite is desired as it can provide an additional strengthening mechanism to the bainitic steel [54]. The process of deformation-induced transformation of the austenite is named as transformation-induced plasticity (TRIP). The local transformation of the retained austenite to martensite hardens the region of the material where the transformation occurs thus preventing further strain in this region. The condition leads to high strain hardening rate of the steel which in the end improve the formability of the bainitic steel.

Figure 33 shows the evolution of the austenite fraction and austenite lattice parameter as a function of quenching temperatures during final quenching stage. In Figure 33, the changes in slope represent the formation of martensite during the final quenching stage which follow the three mentioned isothermal treatments. The temperatures at which this martensite formation is occurred will be named "secondary" *Ms* temperatures. Therefore, Point 1 in Figure 33(a) represents the secondary *Ms* temperature for the isothermal treatment above *Ms*, while Point 2 and 3 represent the *Ms* temperature for isothermal treatment below *Ms* and tempering, respectively. The secondary *Ms* temperatures with its corresponding changes in C-content of the austenite from the three isothermal treatments around *Ms* are summarized in Table 6.

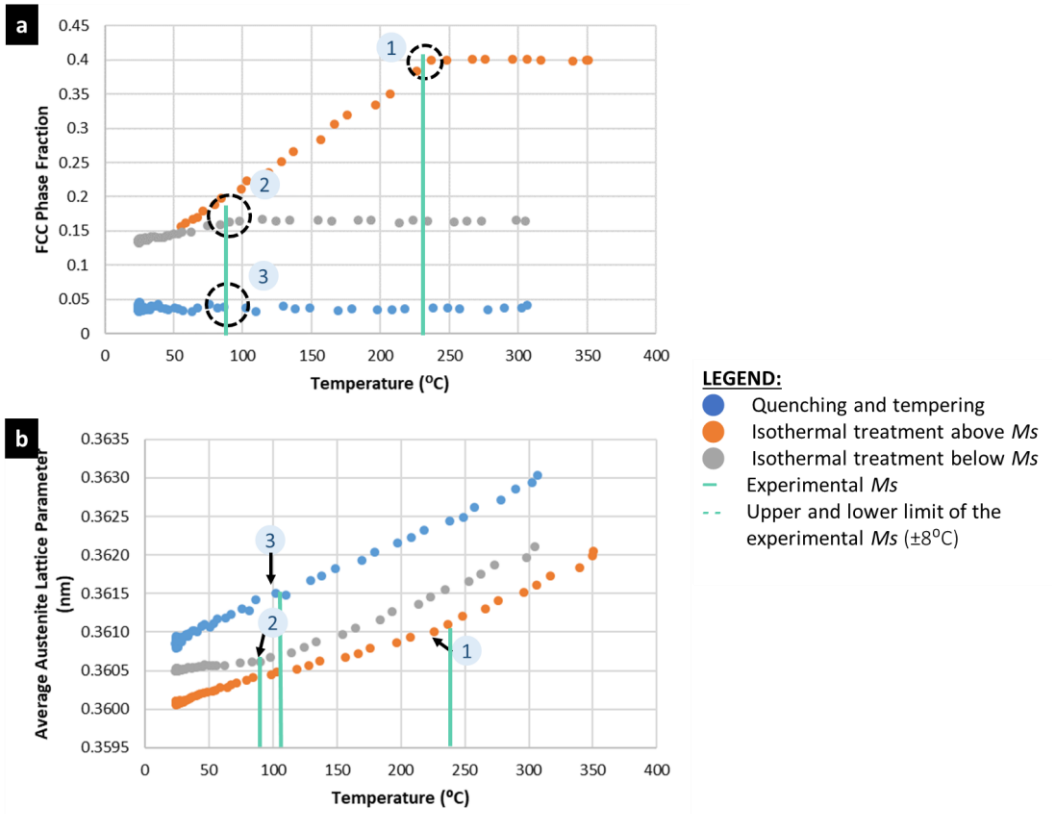

Figure 33 The evolution of a) FCC phase fraction and b) average lattice parameter of the austenite as a function of quenching temperature. The dashed circles represent the point where the estimated Ms temperatures lie.

Table 6 Comparison between secondary Ms temperature and changes in the C-content of the retained austenite measured during the last cooling to the room temperature of the three isothermal treatments performed around Ms temperature.

Point Number	Isothermal Treatment	Secondary *Ms* Temperature (°C)	C-content in the Austenite (wt.%)	
			Initial Isothermal	Final Isothermal
1	Isothermal	240°C ± 8°C	0.10±0.01	0.23±0.01

	Treatment above *Ms*			
2	Isothermal Treatment below *Ms*	77°C ± 8°C	0.07±0.01	0.45±0.01
3	Tempering	77°C ± 8°C	0.22±0.01	0.45±0.01

Table 6 shows that the isothermal treatment above *Ms* has the highest new *Ms* temperature. This condition is expected as in this isothermal treatment, the C-enrichment of the austenite is the lowest (around 0.13 wt.%) which gives rise to least stable austenite.

In addition to that, compared to the tempering treatment which is also performed in the same treatment temperature, isothermal treatment below *Ms* shows the highest C-enrichment of the austenite (Table 6). As mentioned in section 3.3.2, for the tempering treatment the enrichment of the austenite occurred due to C-redistribution process from the martensite. However, this process alone cannot explain the significant increase in the C-content during the isothermal treatment below *Ms* as the martensite present is small (0.034 phase fraction). Therefore, it is suspected that the C-enrichment process of the austenite occurred by simultaneous enrichment from other BCC structures present which is bainite.

4

Conclusions and Recommendations

In this study, phase transformations and carbon redistribution processes were studied during isothermal treatment below *Ms* in low-carbon high-silicon steel. In order to understand the microstructural evolutions occurring in this treatment, three additional treatments were performed: direct quenching, tempering of martensite, and isothermal treatment above *Ms.* These four treatments were studied with the aid from in-situ synchrotron XRD.

4.1 Conclusions

In the isothermally treated sample at a temperature below *Ms*, concurrency of tempering of martensite and bainite formation is expected. Therefore, the details of the microstructural developments during isothermal treatment below *Ms* can be determined by first investigating the microstructural evolutions related to the tempering of martensite and the formation of bainite. The microstructural development for the tempering of martensite were obtained through direct quenching followed by tempering treatment while the microstructural development of bainite formation were collected through isothermal treatment above *Ms*.

1. **Direct quenching followed by tempering treatment (Tempering of martensite)**
   a. Based on the diffractograms obtained during tempering stage, tempering of martensite is identified with carbon partitioning from the martensite to the adjacent austenite.
2. **Isothermal treatment above *Ms* (Bainite formation)**
   a. Bainite formation is correlated with the fluctuations of the austenite lattice parameter at the beginning of the isothermal treatment.
   b. Bainite is suggested to form initially at the austenite region (austenite/austenite interface) with low-C content.
   c. During formation of bainite, it is observed that carbon partitioning from the bainite to the adjacent austenite
3. **Isothermal treatment below *Ms***
   a. The presence of martensite is identified prior to the isothermal treatment below *Ms*.
   b. Bainite was observed to be formed right after the treatment started.
   c. Based on the results from the diffractograms, there are six concurrent processes occurred during isothermal treatment below *Ms* which be divided into three categories:
      – Carbon partitioning from supersaturated BCC phases (bainite and martensite) to austenite
      – Bainite formation: at the austenite/austenite interface and at the martensite/austenite interface
      – Additional carbon redistribution processes

In addition to study the microstructural developments below *Ms*, the data obtained during final quenching stage of the four heat treatments showed that enriching the austenite reduces the *Ms* temperature of the sample.

4.2 Recommendations

The conclusions mentioned previously are obtained only by analysing the data obtained from one characterisation method which is SXRD method. In order to gain a deeper understanding of the microstructural developments below *Ms*, some additional characterization techniques that can be applied for further research:

1. In order to overcome the challenges from the peak finding in the absence of the crystal structure and peak asymmetry, development of a software-routine which can separate the overlapped peaks is needed.
2. Since the carbon quantification in both BCC and FCC structures was calculated based on empirical equations, atom probe tomography (APT) can be performed in order to study the solute redistribution through identifying the local chemical composition around the BCC/FCC interface during isothermal treatment below *Ms*.
3. Since the characterisation of BCC structures during isothermal treatment below *Ms* was done through analysis of the trend in the evolution of BCC lattice parameter, transmission electron microscopy (TEM) is needed. TEM is expected to provide better microscale characterisation especially for identifying the carbon segregation in the dislocation or carbides formation that are included in the carbon redistribution processes from the supersaturated BCC structures (bainite or martensite).
4. In order to study the effect of the stability of retained austenite on the mechanical properties of the steel, mechanical testing such as tensile test is needed to be carried out. By tensile testing samples that contained enriched retained austenite, the relation between C-content and the mechanical stability of the retained in this specific steel alloy can be obtained.
5. In order to study the strains introduced by martensite and bainite, an in-situ $sin^2\varphi$ method is needed. In $sin^2\varphi$ method, the angle between the scattering vector and the surface normal, φ, is varied by tilting the sample around an axis parallel to the plane through the incident and diffracted beam. The experimental setup of this method is presented in Figure 34. By varying treatment temperature, the strain introduced by bainite during isothermal treatments above *Ms* can be calculated. The results from it can be used to study the evolution of the strain during the isothermal treatment below *Ms* which can also be studied using an in-situ $sin^2\varphi$ method.

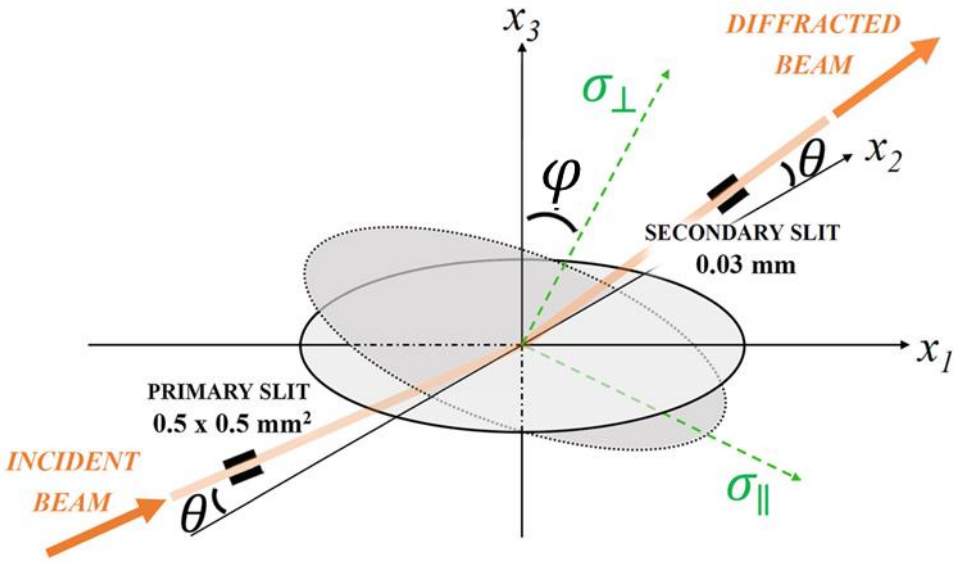

Figure 34 Illustration of the experimental setup of the $sin^2\varphi$ (taken from [52])

Bibliography

[1] P. Manohar and M. Ferry, ‘Thermomechanical processing of ferrous alloys’, *Deform. Process. Struct. Mater.*, pp. 76–125, Jan. 2005.

[2] C. Lesch, N. Kwiaton, and F. B. Klose, ‘Advanced High Strength Steels (AHSS) for Automotive Applications − Tailored Properties by Smart Microstructural Adjustments’, *steel Res. Int.*, vol. 88, no. 10, p. 1700210, Oct. 2017.

[3] O. Bouaziz, H. Zurob, and M. Huang, ‘Driving Force and Logic of Development of Advanced High Strength Steels for Automotive Applications’, *steel Res. Int.*, vol. 84, no. 10, pp. 937–947, Oct. 2013.

[4] N. Fonstein, ‘Evolution of Strength of Automotive Steels to Meet Customer Challenges’, in *Advanced High Strength Sheet Steels: Physical Metallurgy, Design, Processing, and Properties*, Cham: Springer International Publishing, 2015, pp. 1–16.

[5] D. K. Matlock and J. G. Speer, ‘Processing Opportunities for New Advanced High-Strength Sheet Steels’, *Mater. Manuf. Process.*, vol. 25, no. 1–3, pp. 7–13, 2010.

[6] N. Fonstein, ‘Candidates to AHSS of Third Generation: Steels with Carbide-Free Bainite’, in *Advanced High Strength Sheet Steels: Physical Metallurgy, Design, Processing, and Properties*, N. Fonstein, Ed. Cham: Springer International Publishing, 2015, pp. 275–295.

[7] H. K. D. H. Bhadeshia and D. V Edmonds, ‘Bainite in silicon steels: new composition–property approach Part 1’, *Met. Sci.*, vol. 17, no. 9, pp. 411–419, 1983.

[8] J.-C. Hell, M. Dehmas, S. Allain, J. M. Prado, A. Hazotte, and J.-P. Chateau, ‘Microstructure – Properties Relationships in Carbide-free Bainitic Steels’, *ISIJ Int.*, vol. 51, no. 10, pp. 1724–1732, 2011.

[9] H. Bhadeshia and R. Honeycombe, ‘Chapter 6 - Bainite’, in *Steels: Microstructure and Properties (Fourth Edition)*, Fourth Edi., H. Bhadeshia and R. Honeycombe, Eds. Butterworth-Heinemann, 2017, pp. 179–202.

[10] A. K. Sinha, C. Wu, and G. Liu, ‘Steel Nomenclature’, in *Steel Heat Treatment: Metallurgy and Technologies*, First Edit., G. E. Totten, Ed. CRC press, 2007, pp. 13–101.

[11] F. G. Caballero, H. Bhadeshia, K. J. A. Mawella, D. G. Jones, and P. Brown, ‘Design of novel high strength bainitic steels: Part 1’, *Mater. Sci. Technol.*, vol. 17, no. 5, pp. 512–516, 2001.

[12] F. G. Caballero, H. K. D. H. Bhadeshia, K. J. A. Mawella, D. G. Jones, and P. Brown, ‘Design of novel high strength bainitic steels: Part 2’, *Mater. Sci. Technol.*, vol. 17, no. 5, pp. 517–522, 2013.

[13] F. G. Caballero and H. K. D. H. Bhadeshia, ‘Very strong bainite’, *Curr. Opin. Solid State Mater. Sci.*, vol. 8, no. 3, pp. 251–257, 2004.

[14] H. K. D. H. Bhadeshia, ‘Modern Bainitic Steels’, in *Bainite in steels.Theory and Practice*, Third Edit., Maney Publishing, 2015, pp. 367–451.

[15] H. K. D. H. Bhadeshia and S. R. Honeycombe, ‘Bainite’, in *Steels - Microstructure and Properties (4th Edition)*, Elsevier, 2017, pp. 179–202.

[16] H. K. D. H. Bhadeshia, ‘3. Carbide Precipitation’, in *Bainite in steels.Theory and Practice*, Third Edit., Maney Publishing, 2015, pp. 61–83.

[17] H. I. Aaronson, W. T. Reynolds, G. J. Shiflet, and G. Spanos, *Bainite viewed three different ways*, vol. 21. 1990.

[18] Z.-G. Yang and H.-S. Fang, ‘An overview on bainite formation in steels’, *Curr. Opin. Solid State Mater. Sci.*, vol. 9, no. 6, pp. 277–286, 2005.

[19] H. K. D. H. Bhadeshia, *The bainite transformation: Unresolved issues*, vol. 273. 1999.

[20] S. Babu, ‘Bainite’, in *Steel Heat Treatment: Metallurgy and Technologies*, 1st Editio., G. E. Totten, Ed. Boca Raton: CRC press, 2006, pp. 179–201.

[21] A. Navarro-López, J. Hidalgo, J. Sietsma, and M. J. Santofimia, ‘Characterization of bainitic/martensitic structures formed in isothermal treatments below the Ms temperature’, *Mater. Charact.*, vol. 128, pp. 248–256, 2017.

[22] H. K. D. H. Bhadeshia, ‘8. Stress and Strain Effects’, in *Bainite in steels.Theory and Practice*, Third., Maney Publishing, 2015, pp. 218–219.

[23] M. Kang, M.-X. Zhang, and M. Zhu, ‘In situ observation of bainite growth during isothermal holding’, *Acta Mater.*, vol. 54, 2006.

[24] I. B. Timokhina *et al.*, ‘Growth of bainitic ferrite and carbon partitioning during the early stages of bainite transformation in a 2 mass% silicon steel studied by in situ neutron diffraction, TEM and APT’, *J. Appl. Crystallogr.*, vol. 49, no. 2, pp. 399–414, 2016.

[25] S. S. Babu *et al.*, ‘In-situ observations of lattice parameter fluctuations in austenite and transformation to bainite’, *Metall. Mater. Trans. A*, vol. 36, no. 12, pp. 3281–3289, Dec. 2005.

[26] H. J. Stone, M. J. Peet, H. K. D. . Bhadeshia, P. J. Withers, S. S. Babu, and E. D. Specht, ‘Synchrotron X-ray studies of austenite and bainitic ferrite’, *Proc. R. Soc. A Math. Phys. Eng. Sci.*, vol. 464, no. 2092, pp. 1009–1027, 2008.

[27] G. Krauss, *Tempering of martensite in carbon steels*, vol. 2. Woodhead Publishing Limited, 2012.

[28] A. V. Sverdlin and A. R. Ness, ‘Fundamental Concepts in Steel Heat Treatment’, in *Steel Heat Treatment Metallurgy and Technologies*, 1st Editio., G. E. Totten, Ed. CRC press, 2006, pp. 152–153.

[29] W. D. Callister Jr and D. G. Rethwisch, ‘The Structure of Crystalline Solids’, in *Materials Science and Engineering - An Introduction (7th ed.)*, 7th Editio., New York: Elsevier, 2007, pp. 38–71.

[30] F. Hajyakbary, J. Sietsma, G. Miyamoto, T. Furuhara, and M. Santofimia, ‘Interaction of carbon partitioning, carbide precipitation and bainite formation during the Q&P process in a low C steel’, *Acta Mater.*, vol. 104, pp. 72–83, 2016.

[31] H. K. D. H. Bhadeshia and S. R. Honeycombe, ‘Tempering of Martensite’, in *Steels - Microstructure and Properties (4th Edition)*, 2017, pp. 237–270.

[32] J. Speer, D. K. Matlock, B. C. De Cooman, and J. G. Schroth, ‘Carbon partitioning into austenite after martensite transformation’, *Acta Mater.*, vol. 51, no. 9, pp. 2611–2622,

2003.

[33] S. Samanta, P. Biswas, S. Giri, S. Singh, and S. Kundu, *Formation of bainite below the M S temperature: Kinetics and crystallography*, vol. 105. 2016.

[34] E. Pinto da Silva, W. Xu, C. Föjer, Y. Houbaert, J. Sietsma, and R. H. Petrov, 'Phase transformations during the decomposition of austenite below Ms in a low-carbon steel', *Mater. Charact.*, vol. 95, pp. 85–93, 2014.

[35] A. Navarro-López, J. Sietsma, and M. J. Santofimia, 'Effect of Prior Athermal Martensite on the Isothermal Transformation Kinetics Below Ms in a Low-C High-Si Steel', *Metall. Mater. Trans. A*, vol. 47, no. 3, pp. 1028–1039, Mar. 2016.

[36] D. Kim, S.-J. Lee, and B. De Cooman, 'Microstructure of Low C Steel Isothermally Transformed in the M S to M f Temperature Range', *Metall. Mater. Trans. A*, vol. 43, 2012.

[37] D. Kim, J. G. Speer, and B. De Cooman, *Isothermal Transformation of a CMnSi Steel Below the MS Temperature*, vol. 42. 2011.

[38] D. H. Kim, J. G. Speer, and B. C. De Cooman, 'The Isothermal Transformation of Low-Alloy Low-C CMnSi Steels below MS', in *PRICM7*, 2010, vol. 654, pp. 98–101.

[39] M. Santofimia, D. Hanlon, S. M. C. Van Bohemen, L. Zhao, and J. Sietsma, 'Perspectives in high strength steels: interactions between non-equilibrium phases', 2013.

[40] M. Oka and H. Okamoto, 'Swing back in kinetics near M s in hypereutectoid steels', *Metall. Trans.*, vol. 19, pp. 447–452, 1988.

[41] H. Kawata, K. Hayashi, N. Sugiura, N. Yoshinaga, and M. Takahashi, 'Effect of Martensite in Initial Structure on Bainite Transformation', *Mater. Sci. Forum*, vol. 638–642, pp. 3307–3312, 2010.

[42] V. Esin *et al.*, 'In situ synchrotron X-ray diffraction and dilatometric study of austenite formation in a multi-component steel: Influence of initial microstructure and heating rate', *Acta Mater.*, vol. 80, pp. 118–131, 2014.

[43] S. S. Babu, '19 - Application of synchrotron and neutron scattering techniques for tracking phase transformations in steels', in *Phase Transformations in Steels*, vol. 2, E. Pereloma and D. V Edmonds, Eds. Woodhead Publishing, 2012, pp. 588–633.

[44] P. Suwanpinij, 'The synchrotron radiation for steel research', *Adv. Mater. Sci. Eng.*, vol. 2016, 2016.

[45] D. Carmele *et al.*, 'Very Hard Synchrotron X-Ray Radiation as an Advanced Characterization Method Applied to Advanced High-Strength Steels', in *THERMEC 2011 Supplement*, 2012, vol. 409, pp. 660–665.

[46] B. B. He, U. Preckwinkel, and K. L. Smith, 'Fundamentals of Two-Dimensional X-ray Diffraction', *Adv. X-ray Anal.*, vol. 43, no. c, pp. 273–280, 1999.

[47] J. Epp, T. Hirsch, and C. Curfs, 'In situ X-Ray Diffraction Analysis of Carbon Partitioning During Quenching of Low Carbon Steel', *Metall. Mater. Trans. A*, vol. 43, no. 7, pp. 2210–2217, Jul. 2012.

[48] V. I. Savran, S. E. Offerman, and J. Sietsma, 'Austenite Nucleation and Growth Observed on the Level of Individual Grains by Three-Dimensional X-Ray Diffraction

Microscopy', *Metall. Mater. Trans. A*, vol. 41, no. 3, pp. 583–591, Mar. 2010.

[49] S. Babu *et al.*, 'In-Situ Observations of Lattice Parameter Fluctuations', *Metall. Mater. Trans. A*, vol. 36, no. December, pp. 3281-3289 ST-In-Situ Observations of Lattice Pa, 2005.

[50] P. Kolmskog *et al.*, 'Direct Observation that Bainite can Grow Below MS', *Metall. Mater. Trans. A*, vol. 43, no. 13, pp. 4984–4988, Dec. 2012.

[51] S. Allain, G. Geandier, J.-C. Hell, M. Soler, F. Danoix, and M. Gouné, 'Effects of Q&P processing conditions on austenite carbon enrichment studied by in situ high-energy X-ray diffraction experiments', *Metals (Basel).*, vol. 7, no. 7, p. 232, 2017.

[52] M. Villa, F. Niessen, and M. A. J. Somers, 'In Situ Investigation of the Evolution of Lattice Strain and Stresses in Austenite and Martensite During Quenching and Tempering of Steel', *Metall. Mater. Trans. A Phys. Metall. Mater. Sci.*, vol. 49, no. 1, pp. 28–40, 2018.

[53] L. Qian, Q. Zhou, F. Zhang, J. Meng, M. Zhang, and Y. Tian, 'Microstructure and mechanical properties of a low carbon carbide-free bainitic steel co-alloyed with Al and Si', *Mater. Des.*, vol. 39, pp. 264–268, 2012.

[54] N. Fonstein, 'TRIP Steels', in *Advanced high strength sheet steels : Physical metallurgy, design, processing, and properties*, Springer International Publishing, 2015, pp. 185–235.

[55] F. G. Caballero, 'Carbide-free bainite in steels', in *Phase Transformations in Steels. Fundamentals and Diffusion-Controlled Transformations*, vol. 1, Woodhead Publishing, 2012, pp. 436–467.

[56] A. A. Gorni, 'Steel forming and heat treating handbook'.

[57] Y. Hu, 'Phase Transformations in Steels during Quenching and Partitioning Heat Treatment', Delft University of Technology, 2016.

[58] A. P. Hammersley, S. O. Svensson, M. Hanfland, A. N. Fitch, and D. Hausermann, 'Two-dimensional detector software: From real detector to idealised image or two-theta scan', *High Press. Res.*, vol. 14, no. 4–6, pp. 235–248, 1996.

[59] N. H. van Dijk *et al.*, 'Thermal stability of retained austenite in TRIP steels studied by synchrotron X-ray diffraction during cooling', *Acta Mater.*, vol. 53, no. 20, pp. 5439–5447, 2005.

[60] Y. Leng, 'X-Ray Diffraction Methods', in *Materials Characterization*, John Wiley & Sons, Ltd, 2010, pp. 45–77.

[61] J. Hidalgo, R. M. Huizenga, K. O. Findley, and M. J. Santofimia, 'Interplay between metastable phases controls strength and ductility in steels', *Mater. Sci. Eng. A*, vol. 745, pp. 185–194, 2019.

[62] B. Hutchinson *et al.*, 'Microstructures and hardness of as-quenched martensites (0.1–0.5% C)', *Acta Mater.*, vol. 59, no. 14, pp. 5845–5858, 2011.

[63] L. Xiao, Z. Fan, Z. Jinxiu, Z. Mingxing, K. Mokuang, and G. Zhenqi, 'Lattice-parameter variation with carbon content of martensite. I. X-ray-diffraction experimental study', *Phys. Rev. B*, vol. 52, no. 14, p. 9970, 1995.

[64] M. Spittel and T. Spittel, '4.5 Thermal expansion of steel', in *Metal Forming Data of*

Ferrous Alloys - deformation behaviour, H. Warlimont, Ed. Berlin, Heidelberg: Springer Berlin Heidelberg, 2009, pp. 104–110.

[65] S.-J. Lee, M. T. Lusk, and Y.-K. Lee, 'Conversional model of transformation strain to phase fraction in low alloy steels', *Acta Mater.*, vol. 55, no. 3, pp. 875–882, 2007.

[66] S. M. C. Van Bohemen, 'The nonlinear lattice expansion of iron alloys in the range 100–1600 K', *Scr. Mater.*, vol. 69, pp. 315–318, 2013.

[67] P. Huyghe, M. Caruso, J.-L. Collet, S. Dépinoy, and S. Godet, 'Into the quenching & partitioning of a 0.2C steel: An in-situ synchrotron study', *Mater. Sci. Eng. A*, vol. 743, pp. 175–184, 2019.

[68] S. Y. P. Allain *et al.*, 'Internal stresses and carbon enrichment in austenite of Quenching and Partitioning steels from high energy X-ray diffraction experiments', *Mater. Sci. Eng. A*, vol. 710, pp. 245–250, Jan. 2018.

[69] G. A. Thomas, F. Danoix, J. G. Speer, S. W. Thompson, and F. Cuvilly, 'Carbon Atom Re-Distribution during Quenching and Partitioning', *ISIJ Int.*, vol. 54, no. 12, pp. 2900–2906, 2014.

[70] A. Bénéteau, E. Aeby-Gautier, G. Geandier, P. Weisbecker, A. Redjaïmia, and B. Appolaire, 'Tempering of a martensitic stainless steel: Investigation by in situ synchrotron X-ray diffraction', *Acta Mater.*, vol. 81, pp. 30–40, 2014.

[71] M. Koo, P. Xu, Y. Tomota, and H. Suzuki, 'Bainitic transformation behavior studied by simultaneous neutron diffraction and dilatometric measurement', *Scr. Mater.*, vol. 61, no. 8, pp. 797–800, 2009.

[72] S. Kundu, K. Hase, and H. K. D. H. Bhadeshia, 'Crystallographic texture of stress-affected bainite', *Proc. R. Soc. A Math. Phys. Eng. Sci.*, vol. 463, pp. 2309–2328, 2007.

[73] H. K. D. H. Bhadeshia and R. Honeycombe, 'Chapter 1 - Iron and Its Interstitial Solutions', in *Steels: Microstructure and Properties (Fourth Edition)*, Fourth Edi., H. Bhadeshia and R. Honeycombe, Eds. Butterworth-Heinemann, 2017, pp. 1–22.

APPENDIX

A. Treatment-Specific Coefficient Of Thermal Expansion (CTE) Of The Austenite

I. Direct Quenching Treatment

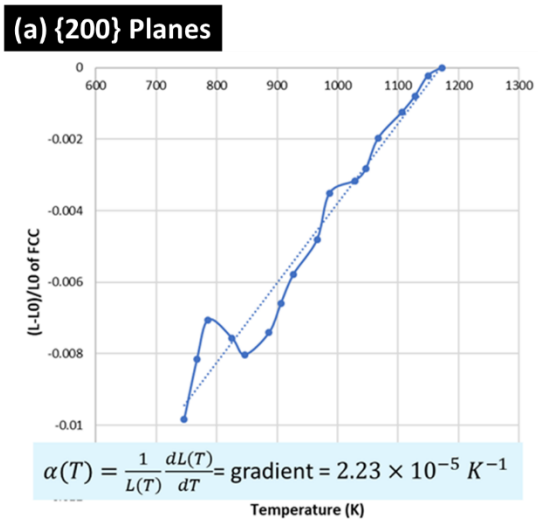

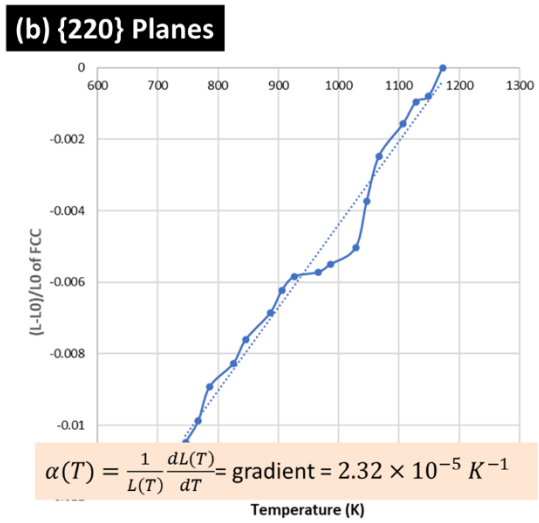

II. Tempering Treatment

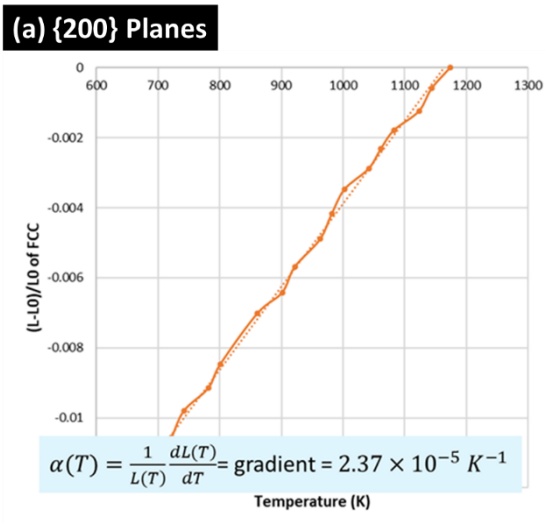

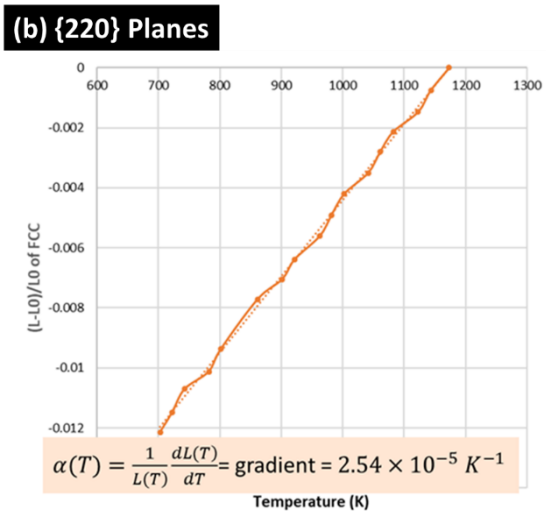

III. ISOTHERMAL TREATMENT ABOVE MS

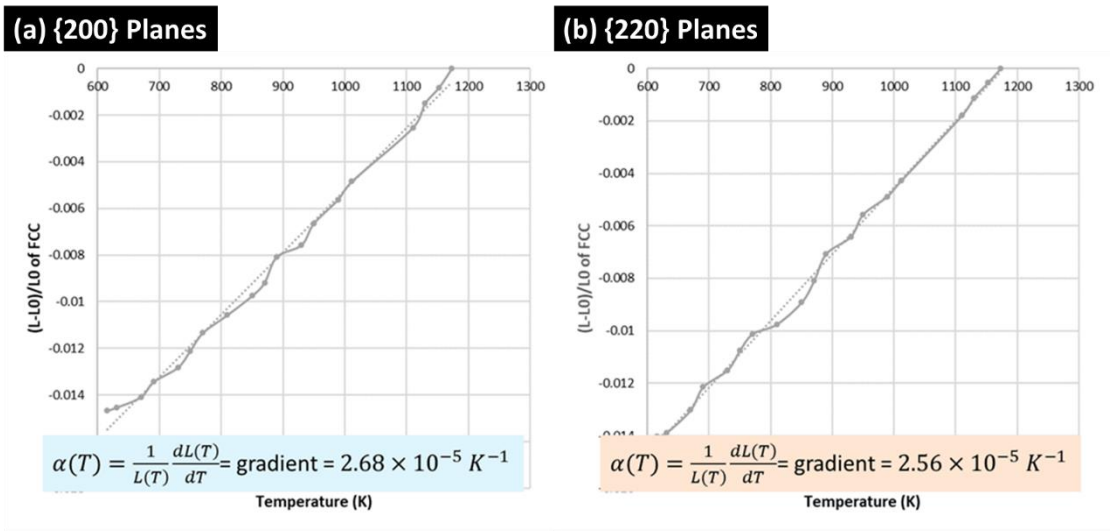

IV. ISOTHERMAL TREATMENT BELOW MS

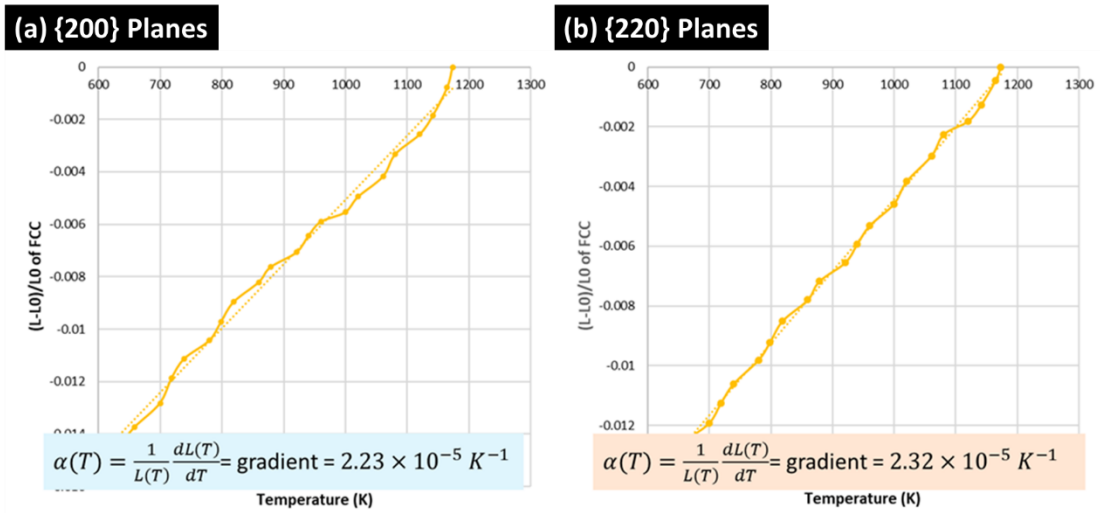

B. Treatment-Specific Coefficient Of Thermal Expansion (CTE) Of The Martensite

I. Direct Quenching Treatment

(a) {200} Planes

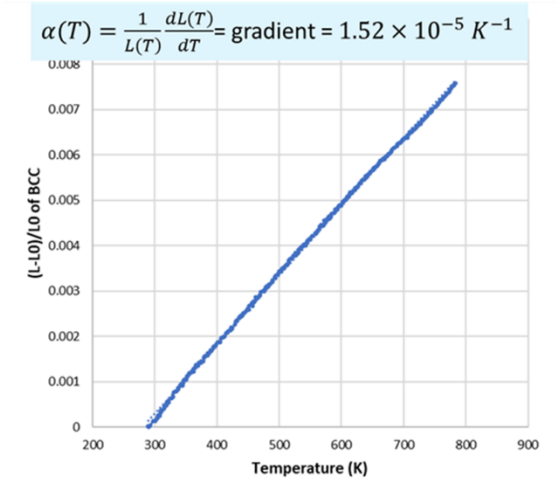

(b) {211} Planes

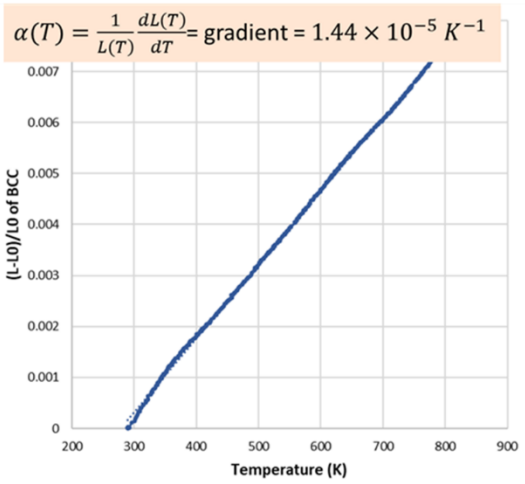

II. Tempering Treatment

(a) {200} Planes

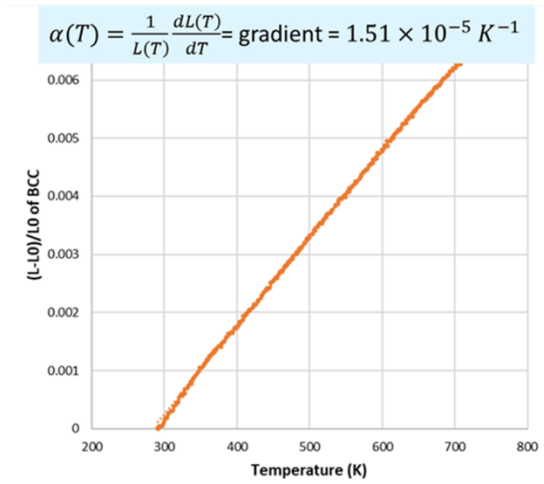

(b) {211} Planes

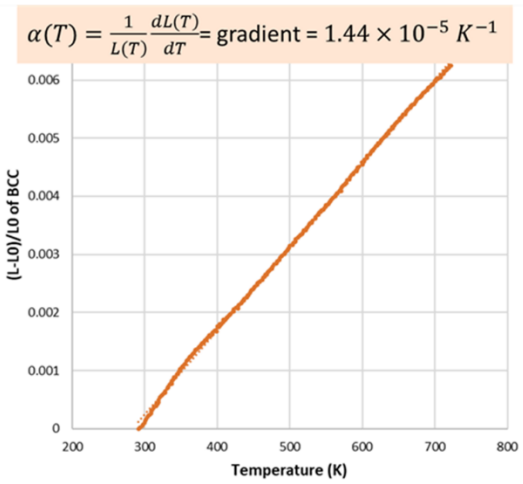

III. ISOTHERMAL TREATMENT ABOVE MS

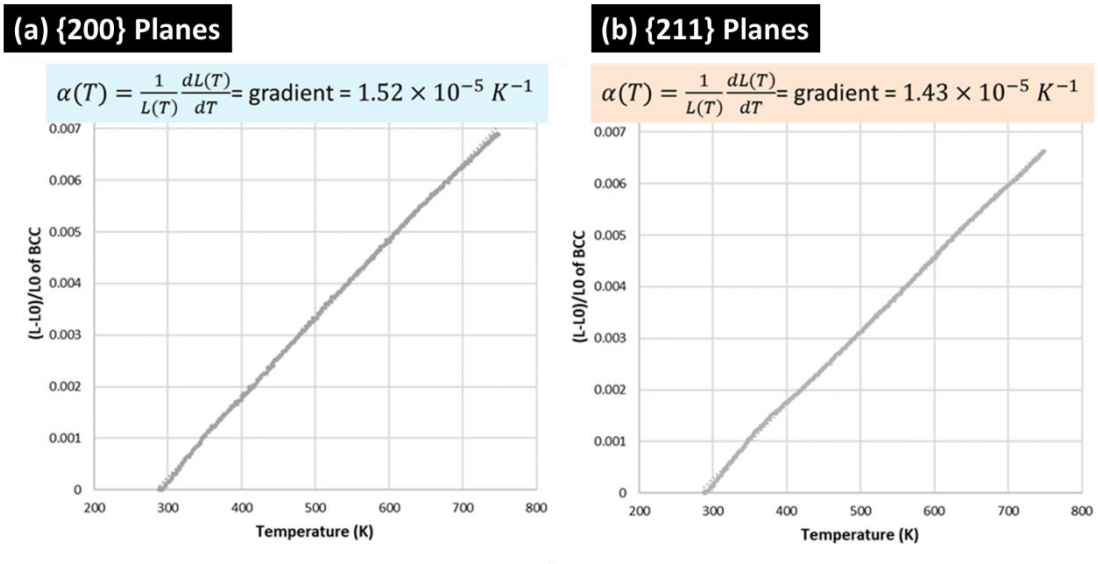

IV. ISOTHERMAL TREATMENT BELOW MS

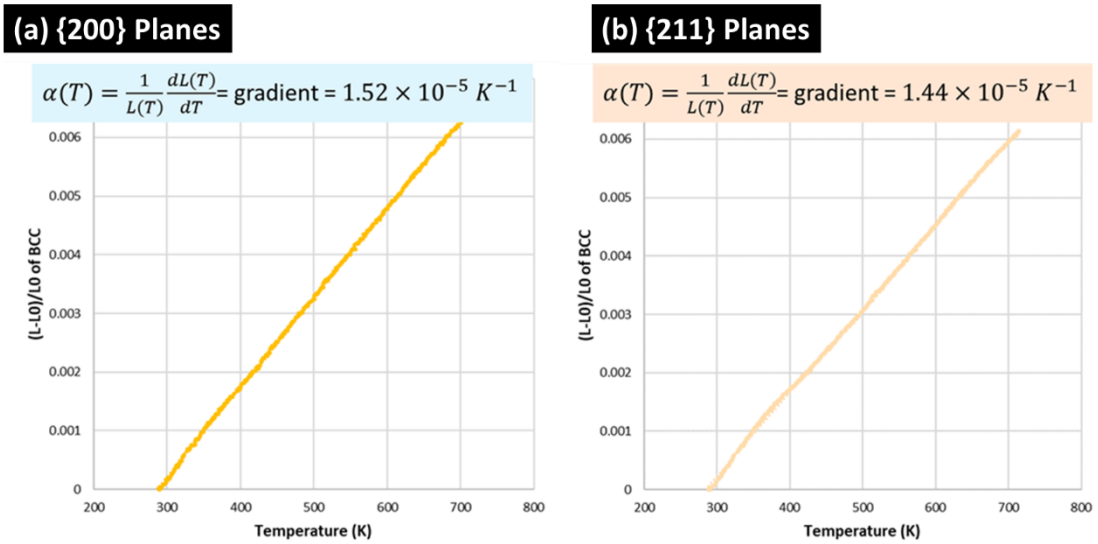

C. TREATMENT-SPECIFIC MS TEMPERATURE

Treatment	Ms (°C)
Direct Quenching	316
Tempering	315
Isothermal Treatment Above Ms	-
Isothermal Treatment Below Ms	327
AVERAGE	**319 ± 8.0**

D. Evolution of The Overall Peak Positions During The Heat Treatments

I. Direct Quenching Treatment

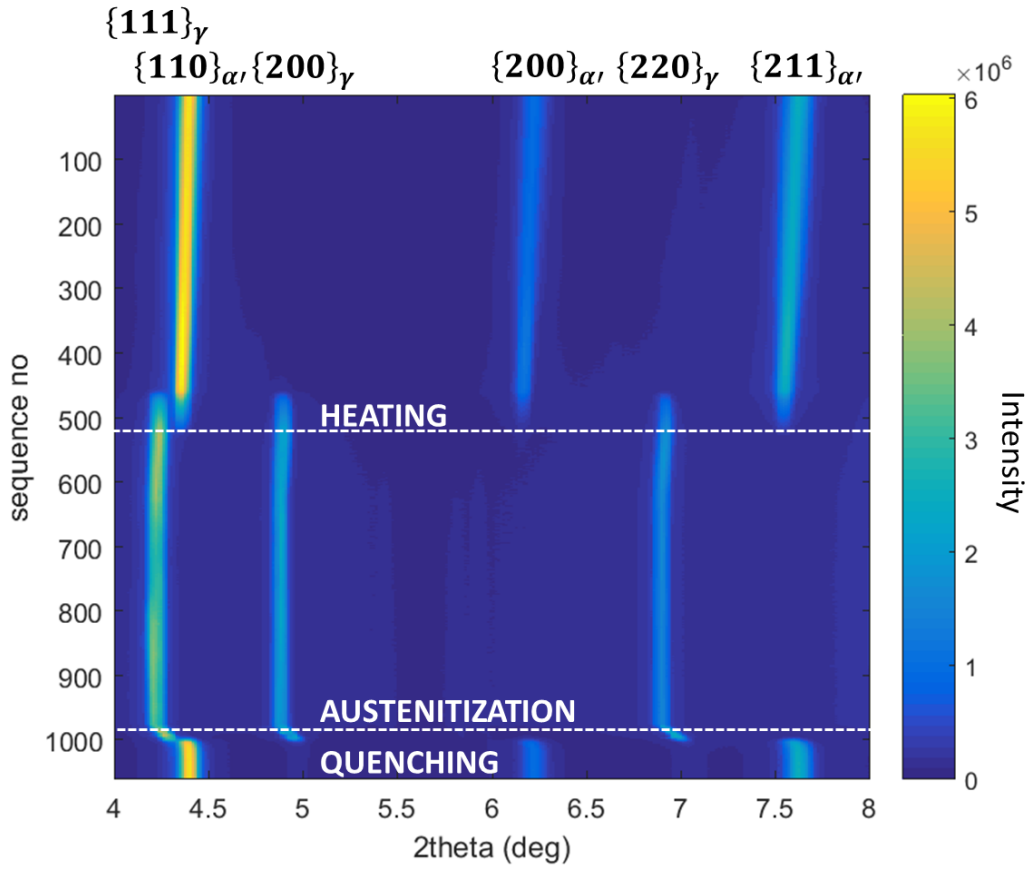

II. TEMPERING TREATMENT

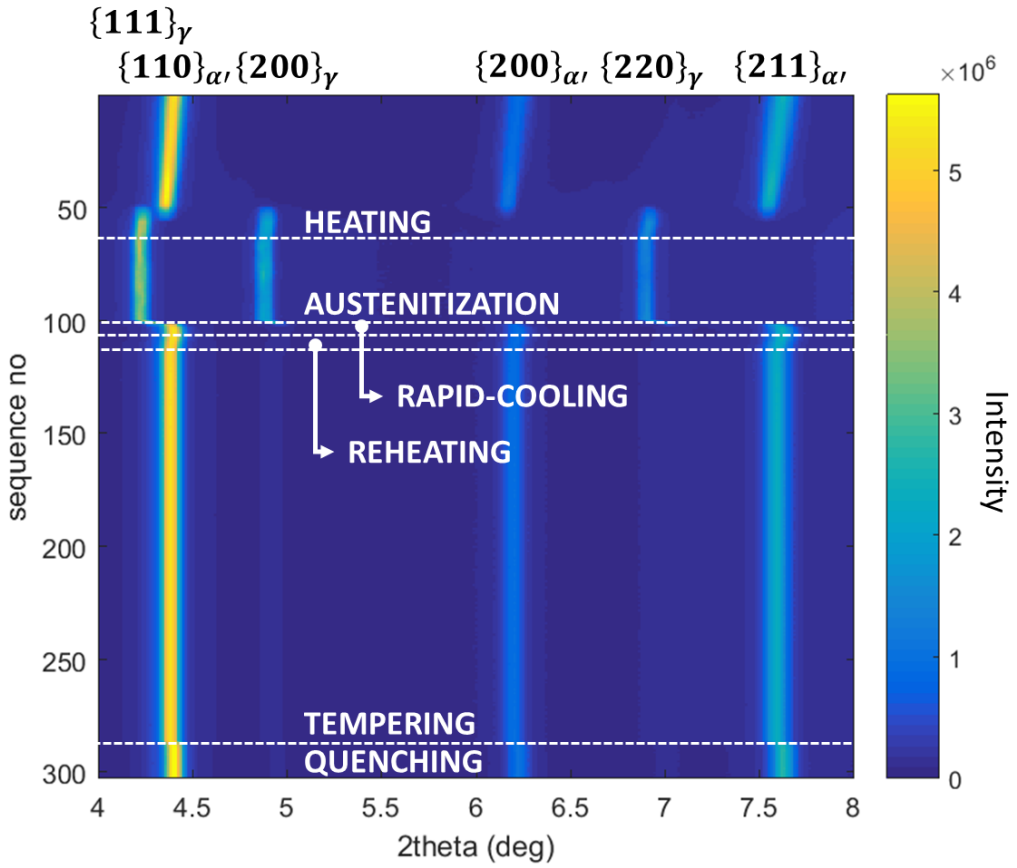

III. ISOTHERMAL TREATMENT ABOVE *MS*

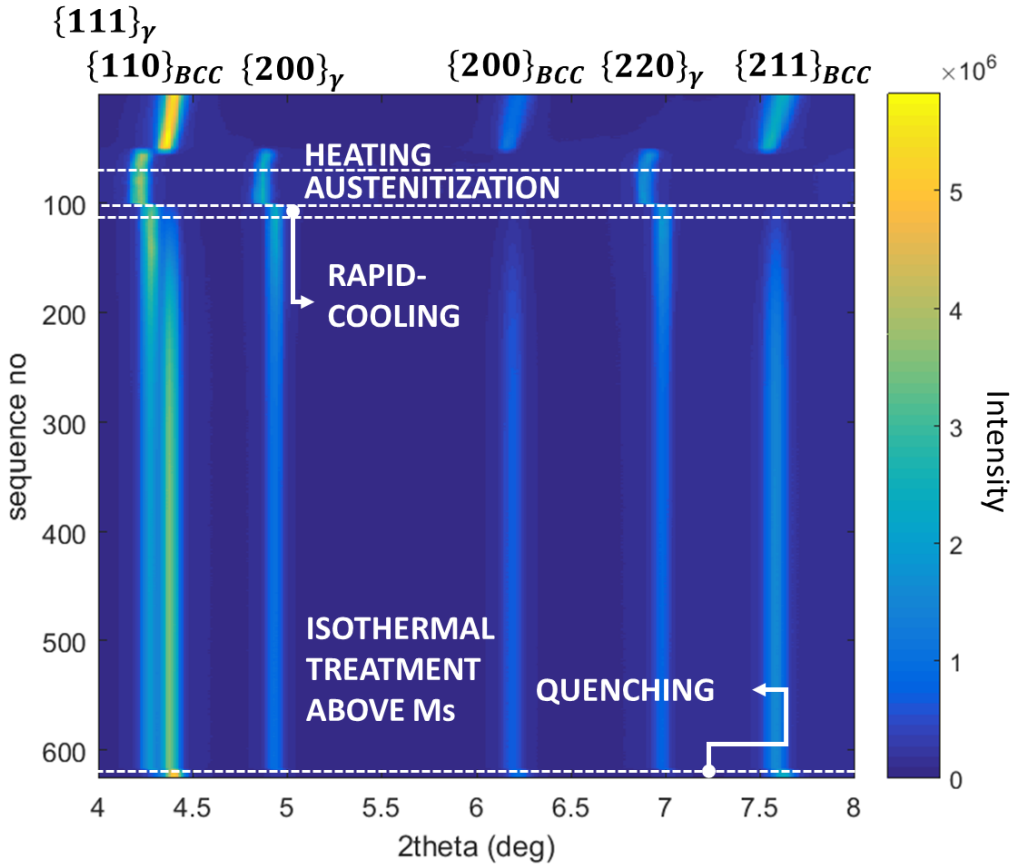

IV. ISOTHERMAL TREATMENT BELOW *MS*

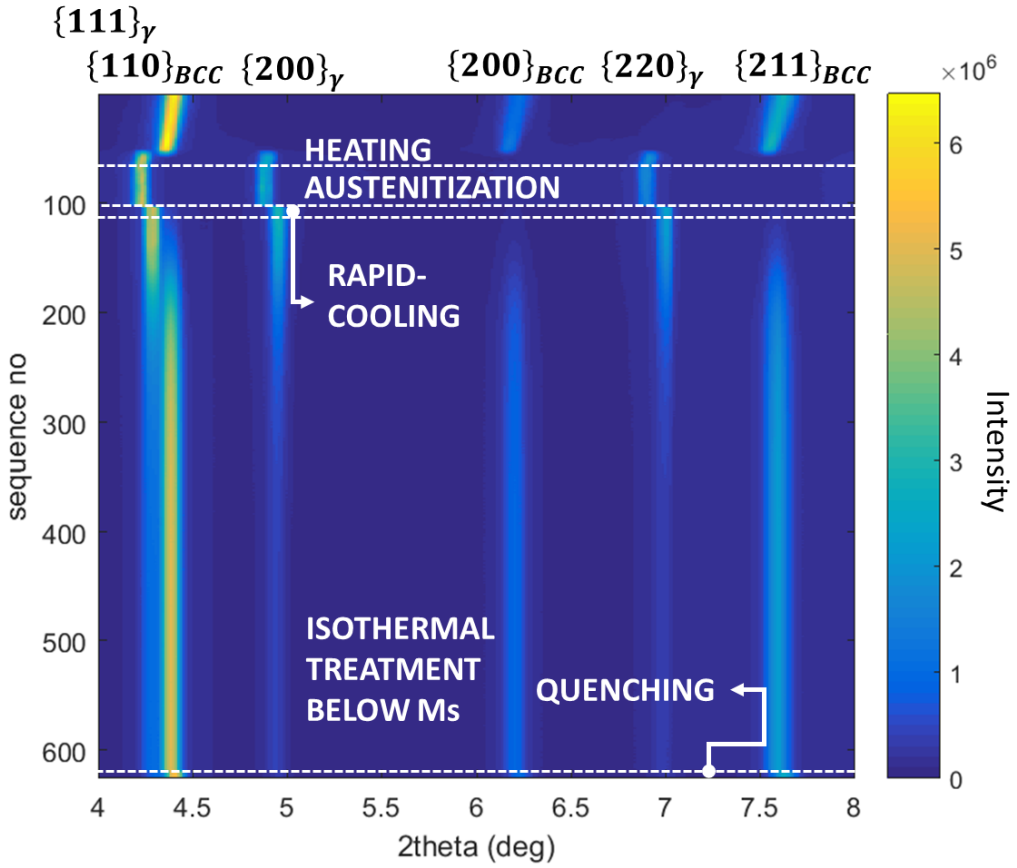

E. Evolution of The Overall Peak Intensity During The Heat Treatments

I. Direct Quenching Treatment

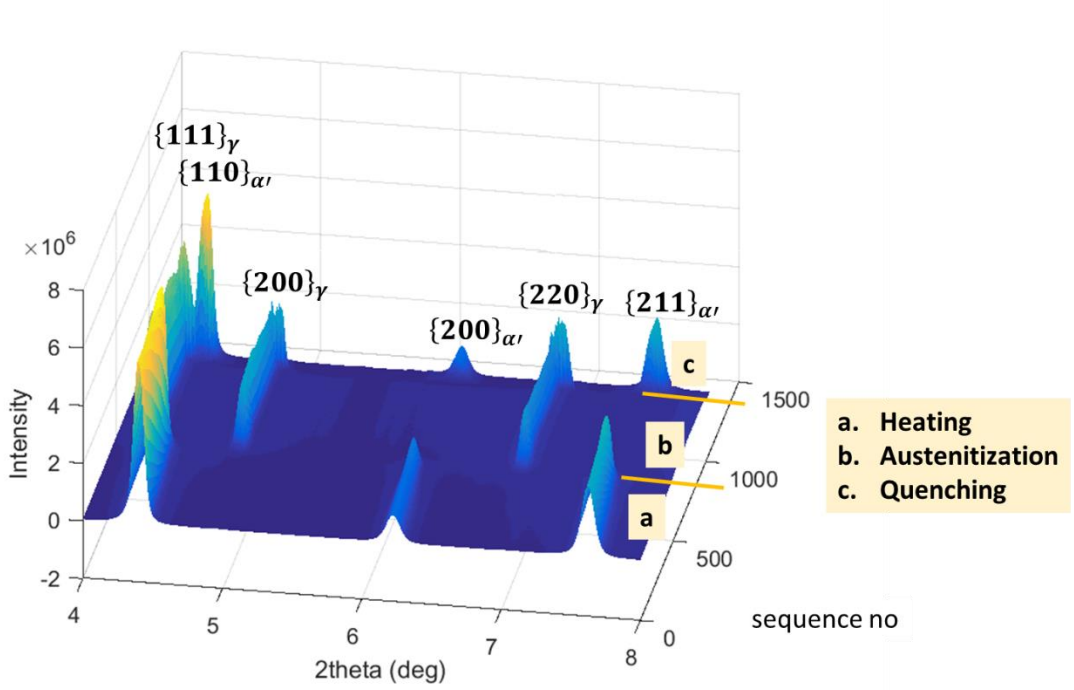

II. Tempering Treatment

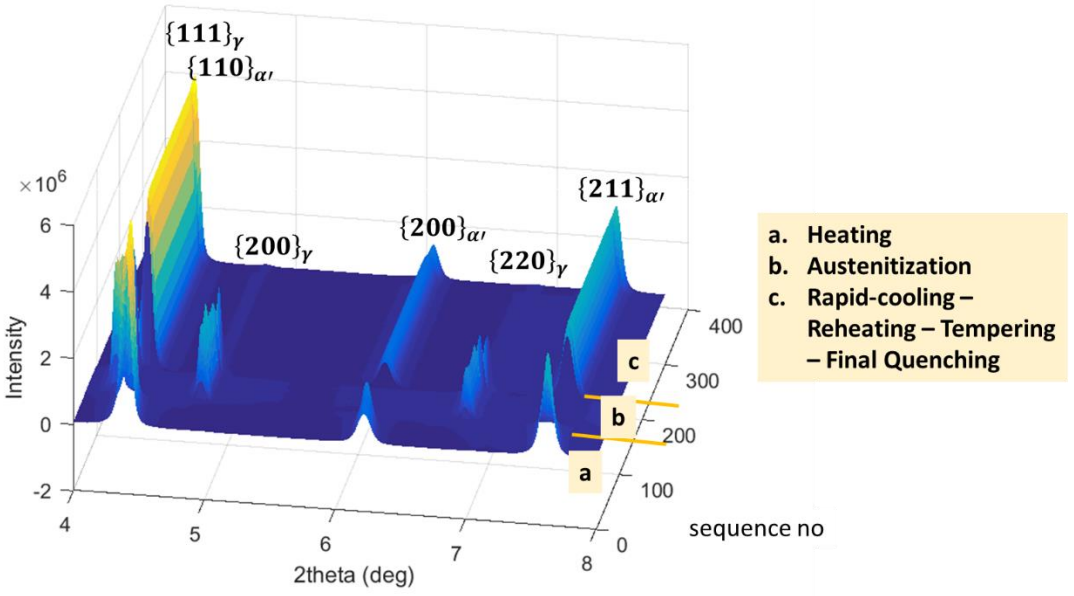

III. ISOTHERMAL TREATMENT ABOVE *MS*

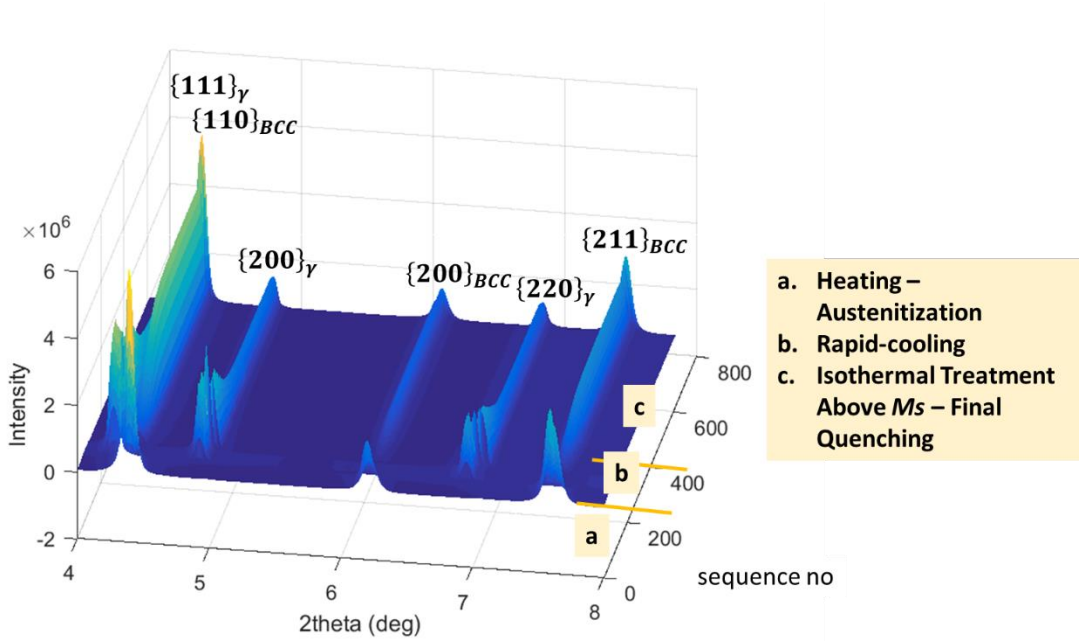

IV. ISOTHERMAL TREATMENT BELOW *MS*